



# AMERICAN METEOROLOGICAL SOCIETY

*Monthly Weather Review*

## **EARLY ONLINE RELEASE**

This is a preliminary PDF of the author-produced manuscript that has been peer-reviewed and accepted for publication. Since it is being posted so soon after acceptance, it has not yet been copyedited, formatted, or processed by AMS Publications. This preliminary version of the manuscript may be downloaded, distributed, and cited, but please be aware that there will be visual differences and possibly some content differences between this version and the final published version.

The DOI for this manuscript is doi: 10.1175/MWR-D-12-00003.1

The final published version of this manuscript will replace the preliminary version at the above DOI once it is available.

If you would like to cite this EOR in a separate work, please use the following full citation:

Newman, J., and P. Heinselman, 2012: Evolution of a Quasi-Linear Convective System Sampled by Phased Array Radar. *Mon. Wea. Rev.* doi:10.1175/MWR-D-12-00003.1, in press.



5 ABSTRACT

6 On 2 April 2010, a quasi-linear convective system (QLCS) moved eastward through Okla-  
7 homa during the early morning hours. Wind damage in Rush Springs, Oklahoma approached  
8 EF1-scale intensity and was likely associated with a mesovortex along the leading edge of  
9 the QLCS. The evolution of the QLCS as it produced its first bow echo was captured by  
10 the National Weather Radar Testbed Phased Array Radar (NWRT PAR) in Norman, Ok-  
11 lahoma. The NWRT PAR is an S-band radar with an electronically steered beam, allowing  
12 for rapid volumetric updates ( $\sim 1$  min) and user-defined scanning strategies. The rapid tem-  
13 poral updates and dense vertical sampling of the PAR created a detailed depiction of the  
14 damaging wind mechanisms associated with the QLCS. Key features sampled by the PAR  
15 include microbursts, an intensifying midlevel jet, and rotation associated with the mesovor-  
16 tex. In this work, PAR data are analyzed and compared to data from nearby operational  
17 radars, highlighting the advantages of using high-temporal-resolution data to monitor storm  
18 evolution.

19 The PAR sampled the events preceding the Rush Springs circulation in great detail.  
20 Based on PAR data, the midlevel jet in the QLCS strengthened as it approached Rush  
21 Springs, creating an area of strong midlevel convergence where it impinged on the system-  
22 relative front-to-rear-flow. As this convergence extended to the lower levels of the storm,  
23 a preexisting azimuthal shear maximum increased in magnitude and vertical extent, and  
24 EF1-scale damage occurred in Rush Springs. The depiction of these events in the PAR data  
25 demonstrates the complex and rapidly changing nature of QLCSs.

# 1. Introduction

A disproportionately large fraction of violent tornadoes are spawned by supercell thunderstorms (e.g., Doswell 2001); however, a significant number of tornadoes are associated with other weather events, such as quasi-linear convective systems (QLCSs). Trapp et al. (2005) found that 18% of all tornadoes during a three-year period occurred within lines, as opposed to supercells or other phenomena such as tropical systems. Furthermore, Trapp et al. (2005) discovered a temporal bias in QLCS tornadoes. While the occurrence of both supercell and QLCS tornadoes peaked at approximately 6 pm local time, QLCS tornado occurrence displayed a secondary peak during the late night and early morning hours, coincident with the tendency for linear storm systems to form after sunset (e.g., Maddox 1983). Since the public is less aware of severe weather warnings at night (e.g., Ashley et al. 2008), this secondary peak in QLCS tornado occurrence presents a significant risk. Furthermore, many nocturnal tornadoes occur without official National Weather Service (NWS) warning, due, in part, to a lack of visual observations (Brotzge and Erickson 2010).

Although QLCS tornadoes tend to be fairly weak, they can reach F2 intensity (Fujita 1971) and cause thousands of dollars in damage (Trapp et al. 2005). QLCS tornadoes can form in many locations along a squall line, presenting a challenge for forecasters trying to issue warnings. In addition, QLCS tornadoes do not typically produce a descending velocity signature in radar data (Trapp et al. 1999). Not surprisingly, it has been suggested that many unwarned tornadoes are associated with linear systems (Brotzge and Erickson 2010).

On 2 April 2010, the National Weather Radar Testbed Phased Array Radar (NWRT PAR, hereafter PAR) in Norman, Oklahoma sampled a low-level circulation associated with a QLCS during the early morning hours. The Weather Forecast Office in Norman did not classify this event as a tornado, primarily because only a large-scale ( $\sim 2$ -km diameter) circulation was sampled by a nearby high-range-resolution X-band radar (KRSP; Junyent et al. 2010); this circulation served to enhance the strong surface winds of the QLCS, but was not considered to fit the classical definition of a tornado (D.L. Andra 2011, personal com-

53 munication). However, these enhanced surface winds coincided with EF1-intensity damage  
54 (e.g., Marshall 2004) in Rush Springs, Oklahoma, as assessed by an independent survey team  
55 (SHAVE 2010).

56 In addition to the PAR research radar, two operational radars sampled the event: the  
57 Weather Surveillance Radar 1988-Doppler (WSR-88D) in Twin Lakes, Oklahoma (KTLX)  
58 and the Terminal Doppler Weather Radar (TDWR) in Norman, Oklahoma. The availability  
59 of radar data with different frequencies and resolutions allows for a unique dataset with  
60 opportunity for comparison. The location of all three central Oklahoma radars, in addition  
61 to the approximate path of the Rush Springs circulation, is shown in Fig. 1. The Rush  
62 Springs circulation was also sampled by one of the CASA radars in southwestern Oklahoma,  
63 KRSP. The reader is referred to Mahale et al. (2012) for a discussion of the Rush Springs  
64 circulation as sampled by KRSP.

65 Much of the previous research regarding QLCS circulations was accomplished during  
66 the Bow Echo and Mesoscale Convective Vortex Experiment in the early 2000s (BAMEX;  
67 Davis et al. 2004). BAMEX researchers utilized airborne radars, mobile wind profilers,  
68 and a variety of other mobile instruments to study the evolution and dynamics of bow  
69 echoes and mesoscale convective vortices. Radar data for BAMEX cases were primarily  
70 derived from two sources: airborne X-band radars and nearby WSR-88Ds. The availability  
71 of two airborne Doppler radar antennas allowed for dual-Doppler analyses. However, a major  
72 disadvantage of the ELDORA airborne radars was the time required to complete each leg of  
73 the scanning strategy (typically 12–13 min; Wakimoto et al. 2006a). The temporal resolution  
74 of WSR-88Ds is also a significant limitation and could preclude adequate sampling of QLCS  
75 circulations. Atkins et al. (2005) noted that several tornadoes produced in association with  
76 the 10 June 2003 St. Louis bow echo had lifetimes shorter than the time required for a  
77 typical WSR-88D volume scan.

78 The PAR sampled the 2 April 2010 Rush Springs circulation with much higher temporal  
79 resolution, completing volume scans approximately every 2 min, compared to every 4.5

80 min for a WSR-88D operating in precipitation mode. In addition, the PAR employed an  
81 oversampled scanning strategy to collect data for the event, providing dense sampling in the  
82 vertical direction. By utilizing high-spatial and temporal resolution, the PAR was able to  
83 sample the evolution of the Rush Springs circulation and the pulse-like nature of the QLCS  
84 in great detail. Analysis of the PAR data suggests that significant changes in QLCSs can  
85 occur on time scales of 2 min or less, and that, as a result, some features of QLCSs are likely  
86 not currently resolved by operational radars.

87 This work focuses on the evolution of the QLCS near Rush Springs as sampled by PAR.  
88 Several rapidly evolving features within the QLCS appeared to affect the strength and for-  
89 mation of the Rush Springs circulation, including a microburst, a strengthening midlevel  
90 jet, and gust front convergence. The evolution of these features is primarily examined using  
91 data from the PAR. In addition, comparisons are made to data collected by the other radars  
92 in central Oklahoma, showing the advantages of using rapid-scan volumetric radar data to  
93 detect significant changes in storm systems.

## 94 **2. Review of QLCS Circulations**

95 Many mature QLCSs contain a strong rear-inflow jet (RIJ; e.g., Smull and Houze 1987),  
96 a region of enhanced winds that travel from the rear to the front of the system in the low-  
97 to-mid troposphere. The RIJ forms when updrafts are tilted upshear over the cold pool and  
98 air from the rear of the storm is accelerated downshear. The effects of baroclinically, cold  
99 pool-generated vorticity, and vorticity generated by the updraft-induced horizontal buoyancy  
100 gradient, combine to accelerate air through the cold pool toward the front of the storm (Fig.  
101 2a).

102 Initially, damaging wind associated with QLCSs was attributed to the descent of the  
103 RIJ to the surface (e.g., Smull and Houze 1987). Detailed WSR-88D analyses and damage  
104 surveys indeed reveal large swaths of damage collocated with the RIJ in several bow echoes

105 (e.g., Wheatley et al. 2006). Other studies have found areas of divergent damage associated  
106 with downbursts and microbursts along the line of storms (Forbes and Wakimoto 1983).  
107 However, many damage surveys have also revealed smaller, convergent, more intense areas  
108 of damage located within or outside the main damage swath (e.g., Fujita 1978, 1981; Forbes  
109 and Wakimoto 1983). Based on numerical simulations, Weisman and Trapp (2003) and  
110 Trapp and Weisman (2003) propose that meso- $\gamma$ -scale vortices, or mesovortices within the  
111 bow echo are responsible for these narrow areas of damage. Several radar-based studies have  
112 confirmed the existence of damage-producing mesovortices in QLCSs (e.g., Atkins et al.  
113 2005, Wakimoto et al. 2006a, Wheatley et al. 2006).

114 Trapp and Weisman (2003) suggest that vorticity couplets form within bow echoes (pref-  
115 erentially north of the bow apex) when baroclinically generated vorticity at the leading  
116 edge of the cold pool is tilted downward by sub-system-scale downdrafts and subsequently  
117 stretched, increasing the resulting vertical vorticity magnitude. When a vortex line asso-  
118 ciated with the cold pool baroclinic vorticity is tilted downward, an anticyclonic vorticity  
119 maximum forms north of the downdraft and a cyclonic vorticity maximum forms south of the  
120 downdraft. In the Trapp and Weisman (2003) simulations, the cyclonic vorticity maximum  
121 eventually dominated as a result of the stretching of planetary vorticity.

122 The Trapp and Weisman (2003) mesovortex formation hypothesis was confirmed by Waki-  
123 moto et al. (2006b), who used an airborne radar to complete a Doppler wind synthesis of  
124 a bow echo on 5 July 2003. However, while Trapp and Weisman (2003) propose that a  
125 precipitating downdraft is the tilting mechanism in mesovortex formation, Wakimoto et al.  
126 (2006b) speculate that a mechanically forced downdraft (e.g., Heymsfield and Schotz 1985)  
127 was responsible for vorticity tilting in the 5 July 2003 case. A schematic model illustrating  
128 this mesovortex genesis process is shown in Fig. 2b.

129 Atkins and St. Laurent (2009) suggest slightly different mesovortex genesis mechanisms.  
130 In quasi-idealized simulations of a bow echo on 10 June 2003 (see Atkins et al. 2005), both  
131 cyclonic vortices and cyclonic/anticyclonic vortex couplets were observed. The cyclonic-only

132 vortices were observed to form at all stages of bow echo evolution. Atkins and St. Laurent  
133 (2009) propose that these cyclonic vortices form when air descending roughly parallel to the  
134 gust front acquires the horizontal vorticity induced by the leading edge of the cold pool. This  
135 horizontal vorticity is subsequently tilted and stretched by an updraft along the gust front. In  
136 contrast, cyclonic/anticyclonic vortex couplets were primarily observed only during the early  
137 bow echo stage. In the simulations, a convective-scale downdraft produced strong outflow  
138 that created an outward bulge in the gust front. This outflow induced a new updraft, which  
139 tilted the vortex lines associated with the cold pool upward, creating a vorticity couplet.

140 As many aspects of QLCS mesovortices are still poorly understood, high-temporal-  
141 resolution sampling by the PAR could provide the opportunity to study these events in  
142 greater detail than what has previously been achieved with operational radars. Heinselman  
143 et al. (2008) showed that examining high-resolution PAR data made it easier to identify  
144 rapidly evolving dynamical features within weather systems, such as strengthening low-level  
145 convergence and vorticity associated with a reintensifying supercell. PAR data could poten-  
146 tially depict previously unresolved features of QLCSs and provide insight into the formation  
147 mechanisms of tornadic mesovortices.

### 148 **3. Synoptic overview**

149 The QLCS occurred during the early morning hours of 2 April 2010 as a strong cold  
150 front moved through central Oklahoma. An upper-level trough also moved through Okla-  
151 homa overnight, adding to the cold frontal forcing. By 1200 UTC, wind speeds had increased  
152 considerably in response to the approaching cold front, increasing the speed shear signifi-  
153 cantly. In addition, backing winds ahead of the front increased low-level directional shear  
154 (see hodograph in Fig. 3b). Based on the 1200 UTC Norman, Oklahoma sounding (Fig.  
155 3b), the magnitude of the surface to 2.5 km wind shear was approximately  $20 \text{ m s}^{-1}$ . (This  
156 sounding was launched at 1100 UTC, so it approximately represents the pre-storm environ-

157 ment.) According to a numerical modeling study by Weisman and Trapp (2003), a low-level  
158 shear value of  $20 \text{ m s}^{-1}$  is sufficient for the formation of bow echoes and the development  
159 of strong mesovortices. However, caution must be used when making comparisons to these  
160 simulations. Weisman and Trapp (2003) used a unidirectional shear profile where wind speed  
161 increases linearly with height in the direction normal to the QLCS; the wind profile from  
162 the Rush Springs QLCS clearly does not fit this model (Fig. 3).

163 By 1200 UTC, the base of the trough was located in southern New Mexico, and much  
164 of western and central Oklahoma was located in a region of strong southwesterly mid- and  
165 upper-level flow associated with the eastern side of the trough. Due to a midlevel jet maxi-  
166 mum, the wind speed increased substantially with height in the 0–6 km layer (Fig. 3b); as a  
167 result, the 0–6 km shear vector magnitude was nearly  $40 \text{ m s}^{-1}$  during the QLCS event. This  
168 shear value is sufficient for long-lived multicellular convection and supercell structures with  
169 midlevel rotation (Rasmussen and Blanchard 1998). The mixed-layer Convective Available  
170 Potential Energy (MLCAPE), calculated using the surface station pressure and the average  
171 temperature and mixing ratio in the lowest 100 hPa of the sounding, was  $1304 \text{ J kg}^{-1}$  from  
172 the 1200 UTC Norman sounding. This value is on the lower end of expected CAPE values  
173 for MCS or bow echo environments (e.g., Weisman 1993; Evans and Doswell 2001).

## 174 4. Event overview

175 As the upper-level trough approached from the west, storms began to form in northwest  
176 Texas, just south of the Oklahoma border, by 0600 UTC. Over the next several hours, these  
177 storms matured and moved eastward into a region of moderate instability. The 0900 UTC  
178 Storm Prediction Center mesoanalysis indicated a region of uncapped  $1000 \text{ J kg}^{-1}$  surface-  
179 based CAPE in central Oklahoma, near the location of Rush Springs (not shown). The  
180 isolated storms grew in both size and intensity as they moved into the narrow corridor of  
181 instability in southwestern Oklahoma. Between 0800 and 1000 UTC, the southern storms

182 increased moderately in strength while additional storms formed rapidly further north in  
183 Oklahoma. The storms in Texas moved northeastward into Oklahoma, forming a QLCS  
184 by 1030 UTC. The initial stages of the QLCS were sampled by KTLX only (Fig. 4a), as  
185 PAR data collection had not yet begun. Between 1055 and 1101 UTC, a bowing segment  
186 developed in the southern portion of the QLCS, causing significant wind damage in the  
187 Rush Springs area; this stage of the QLCS was sampled by the PAR (Fig. 4b) in addition  
188 to KTLX. The QLCS moved eastward through Oklahoma and weakened during the early  
189 morning hours.

190 A damage survey of Rush Springs, Oklahoma was led by Kiel Ortega, a research associate  
191 with the University of Oklahoma Cooperative Institute for Mesoscale Meteorological Studies.  
192 The damage survey team determined that the EF1-scale Rush Springs damage was associated  
193 with a circulation embedded along the leading edge of the QLCS (see Fig. 1 for damage  
194 path). Damage signatures included peeled roof shingles and several rolled-over mobile homes.  
195 Since the storm motion of the QLCS was very fast (at least  $25 \text{ m s}^{-1}$ ), the true intensity  
196 of the Rush Springs circulation is unknown; the motion of the QLCS likely augmented the  
197 circulation intensity substantially.

## 198 **5. PAR data analysis**

199 PAR is an S-band (9.38-cm) research radar located in Norman, Oklahoma. Unlike a  
200 WSR-88D, the PAR operates by using a panel of transmit/receive elements, changing the  
201 phases of the elements to steer the radar beam in azimuth and elevation. Electronic beam  
202 steering offers several potential advantages over conventional mechanical steering, including  
203 a 75% reduction in volumetric scan time (in comparison to a WSR-88D) and the ability  
204 to adaptively scan regions of interest (Zrnić et al. 2007; Heinselman and Torres 2011).  
205 The research PAR used for this study only has one panel of transmit/receive elements and  
206 therefore can only scan one  $90^\circ$  sector at a time (e.g., Fig. 4b). However, an operational

207 PAR would have four panels that could simulataneously scan four  $90^\circ$  sectors at the same  
208 time, producing full volumetric updates in 1–2 min (Heinselman et al. 2008).

209 The transmitted beamwidth of the PAR increases gradually with increasing angle from  
210 boresight (the center of the panel), ranging from  $1.5^\circ$  at boresight to  $2.1^\circ$  at an angle of  
211  $45^\circ$  from boresight. Overlapped azimuthal sampling is used, such that the sampling interval  
212 at a particular location is equal to one half of the beamwidth at that location. The range  
213 resolution of the PAR is 240 m (Zrnić et al. 2007).

#### 214 *a. Sampling strategies*

215 On 2 April 2010, the PAR was operating nearly continuously from 1037 to 1140 UTC, and  
216 during that time used two different scanning strategies. Initially, an oversampled scanning  
217 strategy was employed, which collects data at 22 elevation angles and uses two different  
218 Pulse Repetition Times (PRTs) at the lowest elevation angles to properly place range-folded  
219 echoes. At 1100 UTC, once the QLCS had moved within 120 km of the PAR, a different  
220 scanning strategy was employed. The second scanning strategy also collected data at 22  
221 elevation angles, but a uniform PRT was used for all tilts, allowing for a faster update time.  
222 The average volumetric update times for the two scanning strategies were 2 min and 1.4  
223 min, respectively.

224 The Nyquist velocity of the PAR was  $29.3 \text{ m s}^{-1}$  during the event. Some wind speeds  
225 within the QLCS exceeded  $30 \text{ m s}^{-1}$  at low levels and  $40 \text{ m s}^{-1}$  at mid- and upper-levels,  
226 surpassing the Nyquist velocity. To improve the depiction of velocity signatures within the  
227 QLCS, velocity data were de-aliased manually with the Solo II editing program (Oye et al.  
228 1995).

229 *b. Microburst*

230 The first event sampled by the PAR (1037–1050 UTC) was a microburst  $\sim 110$  km from  
231 the radar that resulted in estimated  $30 \text{ m s}^{-1}$  winds in Cotton County and knocked over  
232 several power poles (NCDC 2010). Golf-ball sized hail also fell in association with the  
233 microburst (NCDC 2010). The location of the microburst damage reports is shown in Fig.  
234 1; the evolution of the microburst as seen in the PAR data corresponds well spatially and  
235 temporally to these reports (Fig. 5).

236 When the PAR began collecting data at 1037 UTC, a high reflectivity core ( $> 65$  dBZ),  
237 indicative of hail, had already elongated and started to descend toward the ground (Fig. 5a).  
238 The reflectivity core initially extended from the lowest PAR scan at  $\sim 1.7$  km above radar level  
239 (ARL) to nearly 8 km ARL. According to an NCDC (2010) report, at approximately 1040  
240 UTC, eight power poles were knocked down in Hulen, Oklahoma as a result of an estimated  
241  $30 \text{ m s}^{-1}$  wind gust. At this time, the reflectivity core associated with the microburst was  
242 still descending. By 1044 UTC, we estimate that the core had almost completely descended  
243 to the ground.

244 The 1044 UTC PAR velocity vertical cross section shows an elevated region of strong  
245 inbound velocities associated with a midlevel jet, centered near  $z = 6$  km (Fig. 5d). In  
246 this cross section, a narrow region of high inbound velocities extends from the midlevel jet  
247 downward to the surface, creating a low-level wind maximum near  $x = 110$  km, just to the  
248 left (southwest) of the wind report in Fig. 5d. The magnitude of this maximum, measured  
249 at 1.6 km ARL by the PAR, was  $30.3 \text{ m s}^{-1}$ , which is quite close to the estimated wind  
250 gust speed in Hulen. In addition, this wind speed is very similar to the radial wind speeds  
251 measured in the midlevel jet by the PAR during this time period. Thus, it appears likely  
252 that high-momentum air was transferred downward from the midlevel jet toward the surface,  
253 possibly in conjunction with the microburst.

254 Golf-ball sized hail ( $\sim 1.75$  in. diameter) was reported at 1050 UTC near Bethel, Ok-  
255 lahoma (NCDC 2010). The location of this hail report corresponds well with the location

256 of the reflectivity core at the end of the microburst’s lifetime (Fig. 5f). Since the lowest  
257 elevation angle of the PAR was sampling the storm  $\sim 1.6$  km ARL at this location, the high  
258 reflectivity core was not sampled as it reached the surface. However, based on the obser-  
259 vations of the reflectivity core in the previous PAR cross sections, we suspect that the core  
260 reached the ground between 1044 and 1050 UTC, producing the golf-ball sized hail reported  
261 in Bethel.

262 *c. Strengthening low-level outflow*

263 The microburst that occurred between 1037 and 1050 UTC appeared to locally strengthen  
264 the outflow along the gust front (Fig. 6a). Soon after 1050 UTC, this area of strengthening  
265 outflow began to extend northwestward and southeastward along the QLCS (Figs. 6b–f).  
266 The reflectivity at the  $0.5^\circ$  elevation angle began to develop into a bowing structure in  
267 response to this surge of outflow, forming a well-defined bow segment by 1054 UTC (Fig.  
268 6c).

269 Although the gust front of the QLCS was not indicated by a typical fine line in reflectivity  
270 imagery (e.g., Wilson et al. 1980), a sharp gradient was present in the  $0.5^\circ$  velocity field (Fig.  
271 6). Several cyclonic azimuthal shear maxima were evident along the gust front; one particular  
272 azimuthal shear maximum, located on the north side of the intensifying outflow, persisted  
273 with time and began to strengthen at approximately 1058 UTC (Fig. 10). The strengthening  
274 of this shear maximum coincided with the formation of a notch in the reflectivity field  
275 (Fig. 6). (As discussed in later sections, this shear maximum was associated with the  
276 mesovortex that contributed to the damage in Rush Springs.) As the strong low-level outflow  
277 extended northwestward along the QLCS, the shear maximum increased in intensity, reaching  
278 a maximum value of  $0.00729 \text{ s}^{-1}$  at 1101 UTC (Fig. 10e). This maximum value occurred  
279 when the strong outflow had extended completely to the location of the shear maximum.  
280 Thus, it is likely that the mechanism that caused the outflow to strengthen along the QLCS  
281 also helped to strengthen the existing azimuthal shear maximum.

282 A series of vertical cross sections taken across different points of the strengthening outflow  
283 indicates that midlevel jet momentum was being transferred to the surface in a similar  
284 method to the momentum transfer that produced the wind gust in Hulen, Oklahoma. An  
285 example of one of these cross sections is shown in Fig. 7 from 1050 to 1104 UTC. At 1052  
286 UTC, a region of velocities exceeding  $30 \text{ m s}^{-1}$  extended from the bottom of the midlevel jet  
287 at  $z \sim 6 \text{ km}$  toward the surface near  $x = 93 \text{ km}$  (Fig. 7b). By 1104 UTC (8 min later), the  
288 extension between the midlevel jet and the area near the surface dissipated, but the high  
289 velocities at the lowest elevation angle remained (Fig. 7h). This process occurred at several  
290 locations along the QLCS as portions of the gust front strengthened and expanded.

291 The initial microburst at 1037 UTC was associated with the first in a series of downward  
292 momentum transfers that caused the low-level winds along the gust front to intensify with  
293 time. The importance of momentum transport in QLCSs was demonstrated by Mahoney  
294 et al. (2009); modeling results suggest that momentum transport can significantly increase  
295 surface winds and affect mesovortex strength.

#### 296 *d. Strengthening midlevel jet*

297 Throughout the 2 April 2010 event, a southwesterly midlevel jet was prominent in Ok-  
298 lahoma, which affected the mid- and low-level flow within the QLCS. As discussed in the  
299 previous section, it is likely that momentum from this midlevel jet descended and strength-  
300 ened the outflow at several locations along the gust front between 1050 and 1101 UTC.  
301 During this time period, the midlevel jet appeared to strengthen and expand in vertical  
302 extent.

303 Because of data quality issues related to range-folding, the midlevel jet was not visible  
304 in the PAR data until 1048 UTC, centered at  $\sim 6 \text{ km}$  above MSL with base velocities of  $30$   
305  $\text{m s}^{-1}$  (Fig. 5e). Initially, a small area of approaching storm-relative velocities was evident  
306 at midlevels; storm-relative velocity magnitudes were  $5\text{--}8 \text{ m s}^{-1}$  in the outer regions of the  
307 jet and  $10\text{--}12 \text{ m s}^{-1}$  in the narrow jet core. Between 1050 and 1052 UTC (Figs. 8a,b), the

308 leading edge of the jet core increased noticeably in both strength and depth. By 1054 UTC  
309 (Fig. 8c), a large region in the jet exhibited storm-relative velocities exceeding  $10 \text{ m s}^{-1}$ .  
310 By 1101 UTC (Fig. 8f), most storm-relative velocity magnitudes in the jet core were 11–14  
311  $\text{m s}^{-1}$ . The strengthening jet created an area of convergence where it met the front-to-rear  
312 inflow (e.g., near  $x \sim 81 \text{ km}$ ,  $z \sim 7 \text{ km}$  in Fig. 8e).

313 *e. Mesovortex circulation*

314 Since only a cyclonic vortex was observed in both PAR and CASA data (Mahale et al.  
315 2012), as opposed to a vorticity couplet, a cyclonic vortex-only mesovortex genesis mechanism  
316 may have taken place, as discussed in the background section (see also Atkins and St. Laurent  
317 2009). Without the use of a numerical simulation or trajectory analysis, it is difficult to  
318 determine source regions for the mesovortex air parcels and the origin of the vertical vorticity  
319 associated with the mesovortex. However, the evolution of the azimuthal shear maximum  
320 associated with the circulation can still be examined using the available PAR data and  
321 related to the dynamics of the QLCS.

322 By 1102 UTC, a moderately strong velocity couplet (maximum velocity difference  $\sim 20$   
323  $\text{m s}^{-1}$ ) associated with the mesovortex was evident in the  $0.5^\circ$  PAR storm-relative motion  
324 field (Fig. 9). At this time, the circulation was located  $\sim 70 \text{ km}$  from the PAR and the  
325  $0.5^\circ$  scan was sampling the circulation  $\sim 0.9 \text{ km ARL}$ . Similar to past studies of bow echo  
326 mesovortices (e.g., Atkins et al. 2005), the circulation was located just north of the bowing  
327 segment (Figs. 6, 9).

328 An azimuthal shear cross section following the path of the developing velocity couplet  
329 from 1052 UTC to 1104 UTC shows a low-level azimuthal shear maximum increase in vertical  
330 extent and magnitude (Figs. 10a–d), reaching a value of  $0.00729 \text{ s}^{-1}$  at 1101 UTC (Fig. 10e),  
331 before tilting downshear and weakening at low levels (Figs. 10f–g). The path of the low-level  
332 shear maximum agrees well with the circulation damage path. In addition, the fluctuations  
333 in the low-level shear magnitude correspond temporally to the development and dissipation

334 of the circulation, as will be discussed in Section 6d. The azimuthal shear vertical cross  
335 sections (Fig. 10) suggest that the circulation developed from the ground up, which is  
336 typical for some nonsupercell tornadoes and circulations (e.g., Wakimoto and Wilson 1989),  
337 particularly those that form in association with a QLCS (Trapp et al. 1999). This ground-up  
338 development is consistent with the tornadic mesovortices studied by Atkins et al. (2005).

339 *f. Enhancement of mesovortex circulation*

340 The strengthening of the midlevel jet and the low-level outflow coincided with the timing  
341 of mesovortex formation, indicated by the strengthening azimuthal shear maximum in the  
342 PAR data (Fig. 10). In this section, it is proposed that convergence associated with the  
343 strengthening midlevel jet served to enhance the existing mesovortex circulation embedded  
344 in the QLCS.

345 Fig. 11 supports the comparison of the convergence field to the location of the jet from  
346 1052 to 1104 UTC. (Damage was occurring in Rush Springs from 1055 to 1104 UTC based  
347 on high-resolution CASA data (Mahale et al. 2012) and damage signatures on the ground  
348 (SHAVE 2010). In Figs. 10 and 11, this approximately corresponds to the area from  $X = 80$   
349 to 65 km.) As the midlevel jet impinged on the front-to-rear system-relative flow, it created  
350 an area of midlevel convergence. We speculate that momentum and convergence associated  
351 with the jet were transported downward (Fig. 11), which may have, in turn, enhanced  
352 the strength of the preexisting surface circulation through vertical vorticity stretching and  
353 vorticity convergence.

354 The Rush Springs mesovortex enhancement is depicted in the azimuthal shear cross  
355 sections in Fig. 10; the azimuthal shear maximum grows taller and narrower as it strengthens  
356 during this same time period. The proximity between this shear maximum and the jet is  
357 evident in Fig. 11e, where the area of strong rotation at the surface at  $x = 70$  km appears to  
358 be located just underneath the leading edge of the midlevel jet. Near the low-level velocity  
359 couplet, an area of strong convergence extended from  $\sim 1$  to 4 km ARL. This evolution

360 suggests that the Rush Springs mesovortex was enhanced by the downward transport of  
361 momentum and convergence associated with the strengthening midlevel jet.

362 The relation between mesovortices and the RIJ has previously been explored for a case  
363 during the BAMEX project. In their study of the 10 June 2003 St. Louis bow echo, Atkins  
364 et al. (2005) noted that tornadic mesovortex genesis appeared to be associated with RIJ  
365 formation and descent. Atkins et al. (2005) suggest that the RIJ can create localized areas  
366 of convergence and strengthen the gust front, promoting stronger vertical vorticity stretching  
367 along the gust front and increasing the likelihood for mesovortex formation. This finding  
368 was verified by Atkins and St. Laurent (2009), who discovered that in model simulations,  
369 the strongest mesovortices formed along gust fronts that were strengthened by a descending  
370 RIJ.

371 It is possible that in the 2 April 2010 case, the midlevel jet played a similar role to the  
372 RIJ of the Atkins et al. (2005) study. Like the tornadic mesovortices studied by Atkins et al.  
373 (2005), the Rush Springs mesovortex formed just north of the midlevel jet as the jet began  
374 to strengthen (Fig. 9) and developed from the ground up (Fig. 10). However, while Atkins  
375 et al. (2005) found that the amount of time between mesovortex genesis and tornadogenesis  
376 was 12 min, on average, for the 10 June 2003 case, PAR data suggest that the time lapse  
377 between genesis times could be much shorter (Fig. 16). More high-temporal-resolution  
378 QLCS data would need to be collected in order to substantiate this claim.

## 379 **6. Comparison to KTLX and TDWR-OKC**

380 The QLCS was also sampled by KTLX, located  $\sim 20$  km northeast of the PAR, and  
381 TDWR-OKC, located  $\sim 6$  km northwest of the PAR (Fig. 1). KTLX is the WSR-88D used  
382 operationally by the NWS office in Norman, Oklahoma. TDWR-OKC serves as a shear  
383 and downburst-detecting radar for airports in the Oklahoma City area and is also used  
384 operationally by the Norman NWS. Both radars sampled the Rush Springs circulation with

385 different temporal and azimuthal resolution than the PAR. In the following sections, key  
386 features of the QLCS, as depicted in the PAR data from the event, will be compared to the  
387 depictions of these features by KTLX and TDWR.

388 *a. KTLX and TDWR sampling strategies*

389 KTLX is an S-band (10-cm) radar with a beamwidth of  $\sim 0.89^\circ$ . KTLX collects data with  
390 an azimuthal sampling interval of  $0.5^\circ$  at the two lowest elevation angles and has an effective  
391 beamwidth of  $\sim 1.02^\circ$  at these elevation angles, as a result of antenna rotation (Brown et al.  
392 2002). At higher elevation angles, the effective beamwidth is  $\sim 1.4^\circ$ . The KTLX range  
393 resolution is 250 m.

394 KTLX was operating continuously throughout the event and used two different scanning  
395 strategies. The first, Volume Coverage Pattern (VCP) 11, collects data at 14 elevation angles  
396 and uses two PRTS for the lowest two elevation angles and one PRT for all other elevation  
397 angles (Brown et al. 2005). At approximately 1115 UTC, when the QLCS was located  $\sim 65$   
398 km from KTLX, the scanning strategy was switched to VCP 12 (Brown et al. 2005). VCP  
399 12 also uses 14 elevation angles, but more elevation angles are focused on the lowest portion  
400 of the atmosphere. The volumetric update times for VCP 11 and 12 are approximately 5  
401 min and 4 min, respectively.

402 In contrast to KTLX and PAR, TDWR-OKC (hereafter TDWR) is a C-band (5-cm)  
403 radar. TDWR only provides Doppler velocity information out to 90 km in range; thus,  
404 TDWR data are only available for the Rush Springs storm starting at approximately 1100  
405 UTC, when the circulation was already causing damage in Rush Springs. Consequently, the  
406 majority of the radar comparisons in this work focus on PAR and KTLX.

407 TDWR has a beamwidth of  $0.55^\circ$ , but the azimuthal resolution is spoiled to  $1^\circ$  due  
408 to a lack of processing power. The TDWR range resolution is 150 m (NOAA, NWS, and  
409 OSTSE 2005). On 2 April 2010, TDWR was operating in hazardous mode, which is used  
410 when potentially severe storms are in range. Each hazardous mode scan consists of one

411 long-range scan to properly place echoes in range and two volumetric scans (with elevation  
412 angles ranging from  $0.5^\circ$  to  $28.2^\circ$ ). Scans at the  $0.5^\circ$  elevation angle are interlaced with the  
413 volumetric updates, so that data at the lowest elevation angle are available every 1 min.  
414 Each hazardous mode scan takes  $\sim 6$  min (NOAA, NWS, and OSTSE 2005).

415 *b. Microburst: PAR and KTLX*

416 PAR sampled the descending reflectivity core associated with the damage-producing  
417 microburst in great detail with six volumetric scans from 1037 UTC to 1050 UTC (Fig. 5).  
418 In contrast, KTLX only sampled the microburst process with three volumetric scans during  
419 this period (Fig. 12). As a result, the descent of the reflectivity core was only visible on  
420 one scan (Fig. 12b). Examination of the 1037 and 1042 UTC scans (Figs. 12a–b) suggests  
421 the descent of high velocity from the midlevel jet toward the ground. By the next scan, at  
422 1047 UTC, the reflectivity core had already descended to the ground and was likely causing  
423 surface wind damage (Fig. 12c). This temporal sampling limitation was also discussed by  
424 Heinselman et al. (2008) for another microburst event.

425 In addition, the location and time of the damage reports did not entirely correspond to  
426 the microburst signatures sampled by KTLX. For example, the golf-ball sized hail report at  
427 1050 UTC was collocated with the reflectivity core as seen in the PAR data (Fig. 5f). This  
428 hail report occurred between KTLX scans; thus, the reflectivity core was only sampled by  
429 KTLX before (Fig. 12c) and after (not shown) the hail report time. Although it is possible  
430 that these damage reports are slightly misplaced in space and/or time (e.g., Witt et al. 1998),  
431 PAR data suggest that this is not the case (Fig. 5).

432 *c. Midlevel jet: PAR and KTLX*

433 The midlevel jet was not as well-sampled by KTLX in comparison to PAR, largely as a  
434 result of coarser vertical sampling. KTLX employed the VCP 11 scanning strategy until 1115

435 UTC, which only features three elevation angles below  $3^\circ$ ; in contrast, the scanning strategies  
436 employed by the PAR collected data at six elevation angles below  $3^\circ$ . This difference in  
437 vertical sampling is evident in vertical cross sections from KTLX and PAR (Fig. 13). The  
438 midlevel jet and lowest part of the storm were sampled at eight elevation angles in the 1052  
439 UTC PAR scan, compared to only four elevation angles in the corresponding KTLX scan. In  
440 the 1052 UTC cross section (Fig. 13b), the strongest region of the midlevel jet (storm-relative  
441 velocities exceeding  $10 \text{ m s}^{-1}$ ) was visible in the PAR data near  $x \sim 100 \text{ km}$ ,  $z \sim 5 \text{ to } 8.5 \text{ km}$ .  
442 In contrast, the strongest part of the jet was only visible in the KTLX data near  $x \sim 126 \text{ km}$ ,  
443  $z \sim 5.5 \text{ to } 8 \text{ km}$  (Fig. 13a); the jet core appeared shallower based on the coarser KTLX data.  
444 In summary, while both PAR and KTLX measured similar storm-relative velocity values in  
445 the midlevel jet, the vertical extent of the jet was resolved better in the PAR data.

446 *d. Mesovortex circulation and enhancement: PAR, KTLX, TDWR*

447 The velocity couplet associated with the mesovortex was evident in the KTLX data, but  
448 the evolution of the azimuthal shear maximum was not depicted in great detail. Fig. 14 shows  
449 a KTLX azimuthal shear cross section taken along the path of the velocity couplet, analogous  
450 to the PAR cross sections in Fig. 10. Between 1052 and 1104 UTC, KTLX completed three  
451 full volume scans, compared to seven PAR volume scans in the same time period. While the  
452 PAR data show the circulation strengthen, grow in height, and subsequently weaken, the  
453 evolution is not as clear in the KTLX data.

454 A time series of maximum low-level LLSD azimuthal shear values derived from all three  
455 central Oklahoma radars before, during, and after the Rush Springs damage time period  
456 (Fig. 15a) further illustrates this point. (Shear was calculated using the local, linear least  
457 squares derivatives (LLSD) method (Smith and Elmore 2004). Note that it is the trends in  
458 azimuthal shear, rather than the actual values, that are important in this case, since LLSD  
459 shear values can vary according to range, radar angle, and beamwidth; Smith and Elmore  
460 2004). The PAR data indicate a gradual increase in azimuthal shear from 1052 UTC to 1101

461 UTC, followed by a slight decrease and another increase at 1106 UTC as the circulation  
462 appeared to reintensify. This reintensification appeared to occur as the leading edge of the  
463 midlevel jet strengthened and began to slope down toward the leading edge of the QLCS,  
464 creating another area of deep, strong convergence (not shown). TDWR, which used low-level  
465 temporal resolution that was similar to PAR, displayed similar trends in the azimuthal shear  
466 field. The KTLX data do not show the evolution of these two azimuthal shear maxima.

467 Fig. 15b shows the temporal evolution of the maximum low-level velocity difference  
468 measured by all three radars. In general, the velocity difference showed a similar temporal  
469 trend to the azimuthal shear — an increase until 1101 UTC, followed by a slight decrease  
470 and another increase at 1106 UTC. However, the TDWR velocity difference values are sig-  
471 nificantly higher than the PAR and KTLX values at nearly every scan time. In addition,  
472 some of the TDWR values represent gate-to-gate velocity differences (e.g.,  $34 \text{ m s}^{-1}$  at 1108  
473 UTC), while the PAR and KTLX maximum and minimum velocities were separated by at  
474 least one azimuth. This discrepancy is likely due to the difference in beamwidth between  
475 TDWR and PAR. TDWR uses a  $1^\circ$  beamwidth with 150 m range resolution while the PAR  
476 beamwidth was  $\sim 1.6^\circ$  at the circulation location with a 240 m range resolution. TDWR  
477 was likely sampling the small-scale, stronger circulation while PAR was sampling the larger-  
478 scale, surrounding circulation. KTLX, with an effective beamwidth of  $\sim 1.02^\circ$  and a range  
479 resolution of 250 m, sampled similar velocity difference values to PAR.

## 480 7. Summary and Conclusions

481 The NWRT PAR sampled the 2 April 2010 QLCS as damage equivalent to an EF1-scale  
482 tornado was occurring in Rush Springs, Oklahoma. This damage appeared to be associated  
483 with a mesovortex that developed and strengthened along the leading edge of the QLCS.  
484 Full volume scans were completed by the PAR approximately every 2 min or less, revealing  
485 the evolution of the QLCS in great detail. In addition, the PAR used a scanning strategy

486 with high vertical resolution, collecting data at 22 elevation angles, compared to only 14  
487 elevation angles used by the nearby WSR-88D in Twin Lakes, Oklahoma.

488 The evolution of the QLCS as it approached Rush Springs and began producing EF1-  
489 scale damage is summarized in Fig. 16. As observed in the PAR data, the microburst  
490 high-reflectivity core reached the ground at approximately 1044 UTC. The microburst ap-  
491 peared to signify the first in a series of momentum transfers from the strengthening midlevel  
492 jet to the ground at several points along the QLCS; as a result of these momentum transfers,  
493 a region of strong low-level outflow developed northwestward along the QLCS, eventually  
494 reaching the location of the Rush Springs circulation. The PAR data suggest that this high  
495 momentum may have provided the strong convergence necessary to strengthen the preexist-  
496 ing mesovortex and cause damage in Rush Springs. At 1052 UTC, the midlevel convergence  
497 began to increase substantially in response to the strengthening jet. Two minutes later, the  
498 low-level shear calculated with the PAR data began to increase, nearly doubling between  
499 1054 and 1101 UTC. One minute after the low-level shear began to increase, the circulation  
500 started causing damage in Rush Springs; the circulation continued to cause damage at the  
501 surface for the next 9 min. The entire process, from the descent of the microburst core to  
502 the end of the wind damage associated with the circulation, took place in approximately 20  
503 min.

504 The rapid evolution of this event highlights the advantages of using rapid-scan volumetric  
505 radar data to depict trends in potentially damaging storms. In addition, it was suggested  
506 that monitoring midlevel features, such as a midlevel jet or RIJ, requires a vast amount of  
507 volumetric data not available with the current WSR-88D network. The increased availability  
508 of volumetric PAR data ensured that the strengthening midlevel jet was well-resolved and  
509 observed in great detail. The PAR data also depicted a descending reflectivity core associ-  
510 ated with a microburst and an intensifying azimuthal shear maximum associated with the  
511 mesovortex. Both these events occurred on very short time scales (5 min or less) and were  
512 therefore not depicted in great detail by KTLX.

513 Data collected by the PAR for the Rush Springs event revealed several potential precur-  
514 sors for damaging circulation formation in QLCSs, such as a strengthening midlevel jet and  
515 strong midlevel convergence. In the future, more rapid-scan volumetric radar data collected  
516 on QLCS cases could further advance the knowledge of mesovortex formation and highlight  
517 additional radar precursors for QLCS circulations.

518 *Acknowledgments.*

519 The authors thank Rick Hluchan for monitoring PAR data collection for the event, Kevin  
520 Manross for assisting with acquisition of TDWR data, Kiel Ortega for supplying damage  
521 survey information, Ami Arthur for assisting with figures, and Jeff Brogden for assisting with  
522 PAR data conversion. Conversations with Dave Andra, Mike Coniglio, and Dusty Wheatley  
523 aided our radar data analysis. Comments from three anonymous reviewers helped improve  
524 the quality of the manuscript. The authors would also like to acknowledge the developers  
525 of NCAR's Solo II radar data editing program and Dennis Flanigan, the developer of the  
526 PAR data translator for Solo II. Funding for the first author was provided by NOAA/Office  
527 of Oceanic and Atmospheric Research under NOAA-University of Oklahoma Cooperative  
528 Agreement NA17RJ1227, U.S. Department of Commerce.

## REFERENCES

- 531 Ashley, W. S., A. J. Krmenc, and R. Schwantes, 2008: Vulnerability due to nocturnal  
532 tornadoes. *Wea. Forecasting*, **23**, 795–807.
- 533 Atkins, N. T. and M. St. Laurent, 2009: Bow echo mesovortices. Part II: Their genesis. *Mon.*  
534 *Wea. Rev.*, **137**, 1514–1532.
- 535 Atkins, N. T., C. S. Bouchard, R. W. Przybylinski, R. J. Trapp, and G. Schmocker, 2005:  
536 Damaging surface wind mechanisms within the 10 June 2003 Saint Louis Bow Echo during  
537 BAMEX. *Mon. Wea. Rev.*, **133**, 2275–2296.
- 538 Brotzge, J. and S. Erickson, 2010: Tornadoes without NWS warning. *Wea. Forecasting*, **25**,  
539 159–172.
- 540 Brown, R. A., V. T. Wood, and D. Sirmans, 2002: Improved tornado detection using sim-  
541 ulated and actual WSR-88D data with enhanced resolution. *J. Atmos. Oceanic Technol.*,  
542 **19**, 1759–1771.
- 543 Brown, R. A., V. T. Wood, R. M. Steadham, R. R. Lee, B. A. Flickinger, and D. Sirmans,  
544 2005: New WSR-88D volume coverage pattern 12: Results of field tests. *Wea. Forecasting*,  
545 **20**, 385–393.
- 546 Davis, C. and Coauthors, 2004: The Bow Echo and MCV Experiment: Observations and  
547 opportunities. *Bull. Amer. Meteor. Soc.*, **85**, 1075–1093.
- 548 Doswell, C. A., III, 2001: Severe convective storms — An overview. *Severe Convective*  
549 *Storms*, Meteor. Monogr., No. 50. 1–26.
- 550 Evans, J. S. and C. A. Doswell, 2001: Examination of derecho environments using proximity  
551 soundings. *Wea. Forecasting*, **16**, 329–342.

552 Forbes, G. S. and R. M. Wakimoto, 1983: A concentrated outbreak of tornadoes, downbursts  
553 and microbursts, and implications regarding vortex classification. *Mon. Wea. Rev.*, **111**,  
554 220–236.

555 Fujita, T. T., 1971: Proposed characterization of tornadoes and hurricanes by area and  
556 intensity. SMRP Res. Paper No. 91, The Univ. of Chicago, Chicago, IL, 42 pp.

557 Fujita, T. T., 1978: Manual of downburst identification for Project NIMROD. SMRP Res.  
558 Paper No. 156, The Univ. of Chicago, Chicago, IL, 104 pp.

559 Fujita, T. T., 1981: Tornadoes and downbursts in the context of generalized planetary scales.  
560 *J. Atmos. Sci.*, **38**, 1511–1534.

561 Heinselman, P. L. and S. M. Torres, 2011: High-temporal-resolution capabilities of the Na-  
562 tional Weather Radar Testbed Phased-Array Radar. *J. Appl. Meteor. Climatol.*, **50**, 579–  
563 593.

564 Heinselman, P. L., D. L. Priegnitz, K. L. Manross, T. M. Smith, and R. W. Adams, 2008:  
565 Rapid sampling of severe storms by the National Weather Radar Testbed Phased Array  
566 Radar. *Wea. Forecasting*, **23**, 808–824.

567 Heymsfield, G. M. and S. Schotz, 1985: Structure and evolution of a severe squall line over  
568 Oklahoma. *Mon. Wea. Rev.*, **113**, 1563–1589.

569 Junyent, F., V. Chandrasekar, D. McLaughlin, E. Insanic, and N. Bharadwaj, 2010: The  
570 CASA Integrated Project 1 networked radar system. *J. Atmos. Oceanic Technol.*, **27**,  
571 61–78.

572 Maddox, R. A., 1983: Large-scale meteorological conditions associated with midlatitude,  
573 mesoscale convective complexes. *Mon. Wea. Rev.*, **111**, 1475–1493.

574 Mahale, V. N., J. A. Brotzge, and H. B. Bluestein, 2012: The analysis of vortices embedded

575 within a quasi-linear convective system using X-band polarimetric radar. *Wea. Forecasting*,  
576 *Accepted*.

577 Mahoney, K. M., G. M. Lackmann, and M. D. Parker, 2009: The role of momentum transport  
578 in the motion of a quasi-idealized mesoscale convective system. *Mon. Wea. Rev.*, **137**,  
579 3316–3338.

580 Marshall, T., 2004: The enhanced Fujita (EF) scale. Preprints, *22nd Conf. on Severe Local*  
581 *Storms*, Hyannis, MA. Amer. Meteor. Soc., 3B.2.

582 NCDC, 2010: Storm Data. Vol. 52, No. 4, 384 pp.

583 NOAA, NWS, and OSTSE, 2005: TDWR Interface Control and Specifications  
584 Documentation for the NWS Supplemental Product Generator. Technical re-  
585 port, National Oceanic and Atmospheric Administration. [Available online at  
586 [www.roc.noaa.gov/SPG/PublicDocs/SPG\\_Product\\_Spec\\_ICD.pdf](http://www.roc.noaa.gov/SPG/PublicDocs/SPG_Product_Spec_ICD.pdf)].

587 Oye, R., C. Mueller, and S. Smith, 1995: Software for radar translation, visualization,  
588 editing, and interpolation. Preprints, *27th Conf. on Radar Meteorology*, Vail, CO. Amer.  
589 Meteor. Soc., 359–364.

590 Rasmussen, E. N. and D. O. Blanchard, 1998: A baseline climatology of sounding-derived  
591 supercell and tornado forecast parameters. *Wea. Forecasting*, **13**, 1148–1164.

592 SHAVE, 2010: Damage Surveys. [Available online at  
593 <http://ewp.nssl.noaa.gov/projects/shave/tornsurveys.php>].

594 Smith, T. M. and K. L. Elmore, 2004: The use of radial velocity derivatives to diagnose  
595 rotation and divergence. Preprints, *11th Conf. on Aviation, Range and Aerospace*, Hyannis,  
596 MA. Amer. Meteor. Soc., P5.6.

597 Smull, B. F. and R. A. Houze, 1987: Rear inflow in squall lines with trailing stratiform  
598 precipitation. *Mon. Wea. Rev.*, **115**, 2869–2889.

599 Trapp, R. J. and M. L. Weisman, 2003: Low-level mesovortices within squall lines and bow  
600 echoes. Part II: Their genesis and implications. *Mon. Wea. Rev.*, **131**, 2804–2823.

601 Trapp, R. J., E. D. Mitchell, G. A. Tipton, D. W. Effertz, A. I. Watson, D. L. Andra, and  
602 M. A. Magsig, 1999: Descending and nondescending tornadic vortex signatures detected  
603 by WSR-88Ds. *Wea. Forecasting*, **14**, 625–639.

604 Trapp, R. J., S. A. Tessendorf, E. S. Godfrey, and H. E. Brooks, 2005: Tornadoes from squall  
605 lines and bow echoes. Part I: Climatological distribution. *Wea. Forecasting*, **20**, 23–34.

606 Wakimoto, R. M. and J. W. Wilson, 1989: Non-supercell tornadoes. *Mon. Wea. Rev.*, **117**,  
607 1113–1140.

608 Wakimoto, R. M., H. V. Murphey, A. Nester, D. P. Jorgensen, and N. T. Atkins, 2006a:  
609 High winds generated by bow echoes. Part I: Overview of the Omaha bow echo 5 July  
610 2003 storm during BAMEX. *Mon. Wea. Rev.*, **134**, 2793–2812.

611 Wakimoto, R. M., H. V. Murphey, C. A. Davis, and N. T. Atkins, 2006b: High winds  
612 generated by bow echoes. Part II: The relationship between the mesovortices and damaging  
613 straight-line winds. *Mon. Wea. Rev.*, **134**, 2813–2829.

614 Weisman, M. L. and R. J. Trapp, 2003: Low-level mesovortices within squall lines and bow  
615 echoes. Part I: Overview and dependence on environmental shear. *Mon. Wea. Rev.*, **131**,  
616 2779–2803.

617 Weisman, M. L., 1992: The role of convectively generated rear-inflow jets in the evolution  
618 of long-lived mesoconvective systems. *J. Atmos. Sci.*, **49**, 1826–1847.

619 Weisman, M. L., 1993: The genesis of severe, long-lived bow echoes. *J. Atmos. Sci.*, **50**,  
620 645–670.

621 Wheatley, D. M., R. J. Trapp, and N. T. Atkins, 2006: Radar and damage analysis of severe  
622 bow echoes observed during BAMEX. *Mon. Wea. Rev.*, **134**, 791–806.

- 623 Wilson, J., R. Carbone, H. Baynton, and R. Serafin, 1980: Operational application of mete-  
624 orological Doppler radar. *Bull. Amer. Meteor. Soc.*, **61**, 1154–1168.
- 625 Witt, A., M. D. Eilts, G. J. Stumpf, E. D. W. Mitchell, J. T. Johnson, and K. W. Thomas,  
626 1998: Evaluating the performance of WSR-88D severe storm detection algorithms. *Wea.*  
627 *Forecasting*, **13**, 513–518.
- 628 Zrnić, D. S. and Coauthors, 2007: Agile-beam phased array radar for weather observations.  
629 *Bull. Amer. Meteor. Soc.*, **88**, 1753–1766.

## List of Figures

- 630
- 631 1 Location of central Oklahoma radars discussed in the text. Path of Rush  
632 Springs circulation is denoted by thick black line, with approximate times as  
633 indicated. Wind and hail reports associated with the first microburst are also  
634 shown. 31
- 635 2 a) Final stage in the formation of an idealized bow echo. Circles with arrows  
636 indicate the sense of environmental and baroclinic vorticity. Black lines in bot-  
637 tom right corner of figure indicate environmental vertical wind shear. Vertical  
638 lines indicate precipitation and shaded area indicates cold pool. Solid white  
639 line denotes front-to-rear flow and black dotted line denotes rear-to-front in-  
640 flow. From Weisman (1992). b) Conceptual model of mesovortex generation  
641 along outflow boundary of 5 July 2003 Omaha bow echo. The vortex tube  
642 in the bottom right shows how a downdraft tilted baroclinically generated  
643 vorticity, forming a vertical vorticity couplet. The vortex tube is oriented in  
644 a north-south direction and is directed toward the south. From Wakimoto  
645 et al. (2006b). 32
- 646 3 Soundings from a) 0000 UTC and b) 1200 UTC on 2 April 2010 from Norman,  
647 OK. Pressure is plotted in hPa and temperature is plotted in °C. Wind barbs  
648 are shown in units of  $\text{m s}^{-1}$ , with one whole barb equal to  $5 \text{ m s}^{-1}$  and one  
649 pennant equal to  $25 \text{ m s}^{-1}$ . Hodographs for wind observations in the lowest  
650 six kilometers of soundings are shown to the right, with wind speeds shown  
651 in  $\text{m s}^{-1}$  and small numbers indicating height above ground level. 33
- 652 4 a) KTLX  $0.5^\circ$  reflectivity at 1037 UTC 2 April 2010. b) PAR  $0.5^\circ$  reflectivity  
653 at 1058 UTC 2 April 2010. In b), dashed line shows cross section location  
654 discussed in PAR analysis section. In both images, Oklahoma counties are  
655 outlined in green, and range rings for each radar are shown in increments of  
656 50 km. 34

- 657 5 PAR northeast-southwest reflectivity (left) and velocity (right) vertical cross  
658 sections. Location of cross section shown in Fig. 4. Decreasing numbers on  
659 the x-axis indicate distance from the PAR in km. Blue and green circles denote  
660 approximate locations of wind and hail reports, respectively, as discussed in  
661 the text. a) 10:37:34 UTC b) 10:39:39 UTC c) 10:41:19 UTC d) 10:44:07 UTC  
662 e) 10:48:17 UTC f) 10:50:14 UTC on 2 April 2010. 35
- 663 6 PAR  $0.5^\circ$  reflectivity (left) and velocity (right) PPI scans. Oklahoma counties  
664 are outlined in green and range rings for the PAR are shown in increments  
665 of 50 km, with the first range ring corresponding to a range of 50 km. In  
666 velocity images, white circles indicate intensifying outflow. Radial spikes seen  
667 in images are the result of sidelobe echoes. White arrow in e) denotes location  
668 of cross section in Fig. 7. a) 10:50:14 UTC b) 10:52:14 UTC c) 10:54:17 UTC  
669 d) 10:56:22 UTC e) 10:58:27 UTC f) 11:01:02 UTC. 36
- 670 7 PAR northeast-southwest velocity vertical cross sections. Decreasing numbers  
671 on the x-axis indicate distance from the PAR in km. Location of cross section  
672 is shown in Fig. 6e. 37
- 673 8 PAR northeast-southwest storm-relative motion vertical cross section. Lo-  
674 cation of cross section shown in Fig. 4. Decreasing numbers on the x-axis  
675 indicate distance from the PAR in km. a) 10:50:14 UTC b) 10:52:14 UTC c)  
676 10:54:17 UTC d) 10:56:22 UTC e) 10:58:27 UTC f) 11:01:02 UTC. 38
- 677 9 PAR  $0.5^\circ$  reflectivity (top left),  $0.5^\circ$  storm-relative motion (top right), and  
678  $3.07^\circ$  storm-relative motion (bottom left) PPI scans at 11:01:02 UTC. Dashed  
679 line shows location of cross sections in Figs. 10 and 11 at 11:01:02 UTC.  
680 Range rings for the PAR are shown in white and Rush Springs circulation is  
681 indicated by white circle in  $0.5^\circ$  storm-relative motion image. At this time,  
682 the  $3.07^\circ$  elevation angle was sampling the QLCS at  $\sim 4.2$  km ARL. 39

- 683 10 PAR northeast-southwest oriented azimuthal shear vertical cross section. Shear  
684 was calculated using the local, linear least squares derivatives (LLSD) method  
685 (Smith and Elmore 2004). Location of cross section at 1101 UTC shown in  
686 Fig. 9. Cross section was centered on azimuthal shear maximum and taken  
687 along the radar beam axis. Decreasing numbers on the x-axis indicate dis-  
688 tance from the PAR in km. White oval indicates approximate region where  
689 azimuthal shear exceeds  $0.002 \text{ s}^{-1}$ . a) 10:52:14 UTC b) 10:54:17 UTC c)  
690 10:56:22 UTC d) 10:58:27 UTC e) 11:01:02 UTC f) 11:02:27 UTC g) 11:03:52  
691 UTC. 40
- 692 11 PAR northeast-southwest oriented storm-relative motion (left) and divergence  
693 (right) vertical cross sections. Location of cross section at 1101 UTC shown  
694 in Fig. 9. Cross section was centered on azimuthal shear maximum and  
695 taken along the radar beam axis. Decreasing numbers on the x-axis indicate  
696 distance from the PAR in km. Divergence was calculated using the LLSD  
697 method (Smith and Elmore 2004). White oval indicates approximate region  
698 where divergence is less than  $-0.001 \text{ s}^{-1}$ . a) 10:52:14 UTC b) 10:54:17 UTC c)  
699 10:56:22 UTC d) 10:58:27 UTC e) 11:01:02 UTC f) 11:02:27 UTC g) 11:03:52  
700 UTC. 41
- 701 11 (continued) 42
- 702 12 As in Fig. 5, but for KTLX radar. Decreasing numbers on the x-axis indicate  
703 distance from KTLX in km. a) 10:37:54 UTC b) 10:42:48 UTC c) 10:47:41  
704 UTC. 43
- 705 13 KTLX and PAR northeast-southwest storm-relative motion vertical cross sec-  
706 tions. Location of cross section shown in Fig. 4. Decreasing numbers on the  
707 x-axis indicate decreasing distance from the radars in km. Times refer to time  
708 of  $0.5^\circ$  elevation scan. a) KTLX, 10:52:35 UTC b) PAR, 10:52:14 UTC. 44

- 709 14 As in Fig. 10, but for KTLX azimuthal shear. Decreasing numbers on the  
710 x-axis indicate distance from KTLX in km. a) 10:52:35 UTC b) 10:57:25 UTC  
711 c) 11:02:20 UTC. 45
- 712 15 Time series of maximum  $0.5^\circ$  a) azimuthal shear and b) velocity difference  
713 values along circulation path from PAR, KTLX and TDWR data. Maximum  
714 velocity difference was found by calculating the difference between the max-  
715 imum and minimum velocity values at constant range within a 3-km search  
716 radius of each point. Black line indicates approximate circulation damage  
717 period. At 1102 UTC, the  $0.5^\circ$  elevation angles of PAR, KTLX, and TDWR  
718 were sampling the circulation at 0.9 km, 1.2 km, and 0.9 km ARL, respectively. 46
- 719 16 Diagram depicting evolution of Rush Springs circulation as observed in PAR  
720 data. Time increases toward the bottom of the diagram.  $\Delta t$  is the time  
721 elapsed between the start times of subsequent radar-indicated signatures. 47

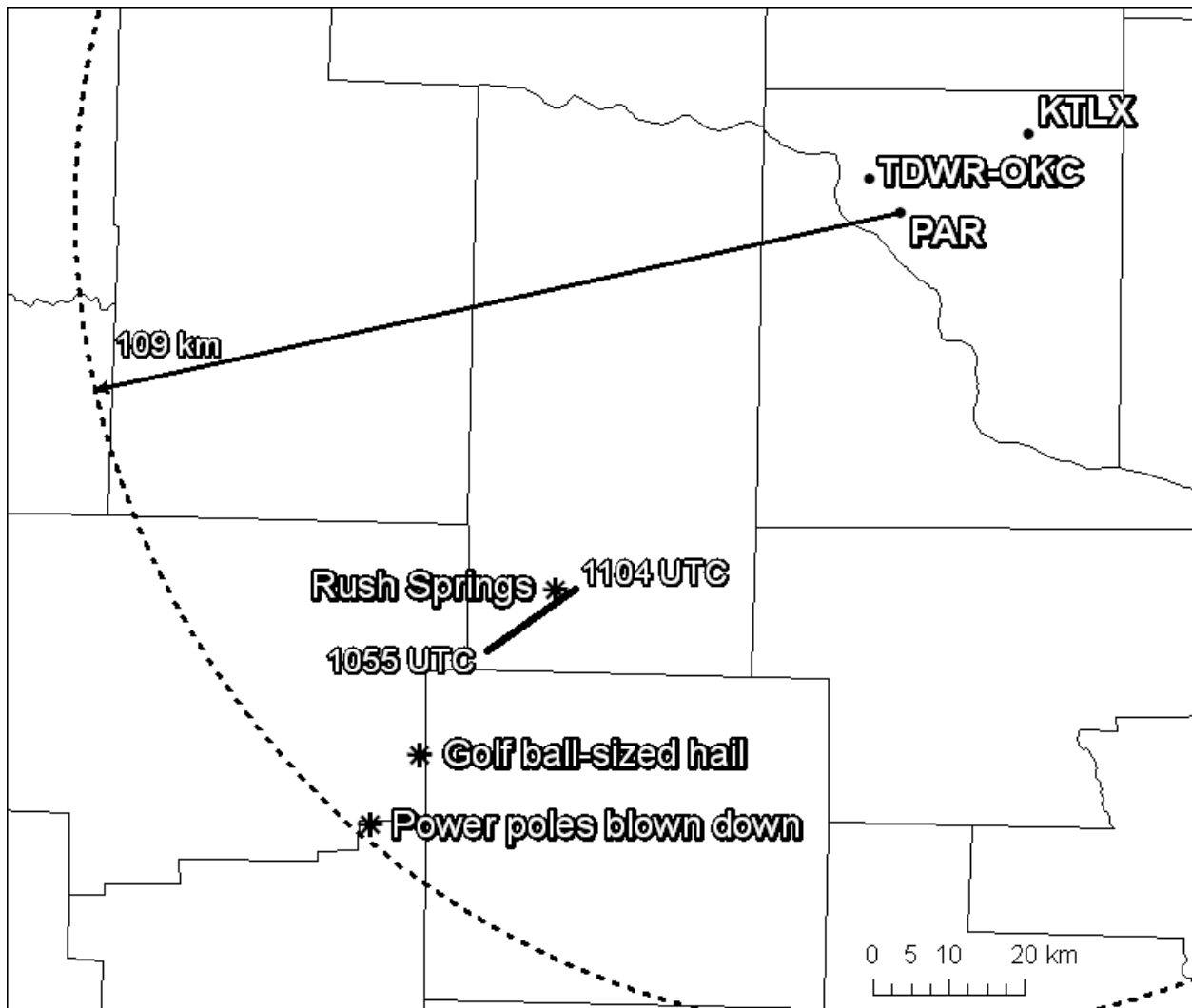


FIG. 1. Location of central Oklahoma radars discussed in the text. Path of Rush Springs circulation is denoted by thick black line, with approximate times as indicated. Wind and hail reports associated with the first microburst are also shown.

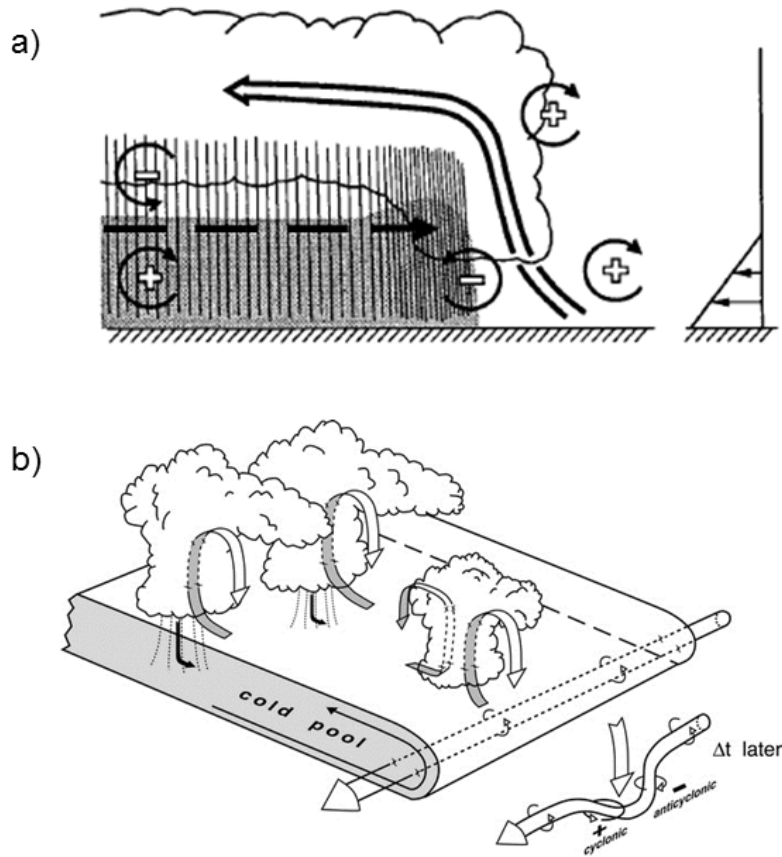


FIG. 2. a) Final stage in the formation of an idealized bow echo. Circles with arrows indicate the sense of environmental and baroclinic vorticity. Black lines in bottom right corner of figure indicate environmental vertical wind shear. Vertical lines indicate precipitation and shaded area indicates cold pool. Solid white line denotes front-to-rear flow and black dotted line denotes rear-to-front inflow. From Weisman (1992). b) Conceptual model of mesovortex generation along outflow boundary of 5 July 2003 Omaha bow echo. The vortex tube in the bottom right shows how a downdraft tilted baroclinically generated vorticity, forming a vertical vorticity couplet. The vortex tube is oriented in a north-south direction and is directed toward the south. From Wakimoto et al. (2006b).

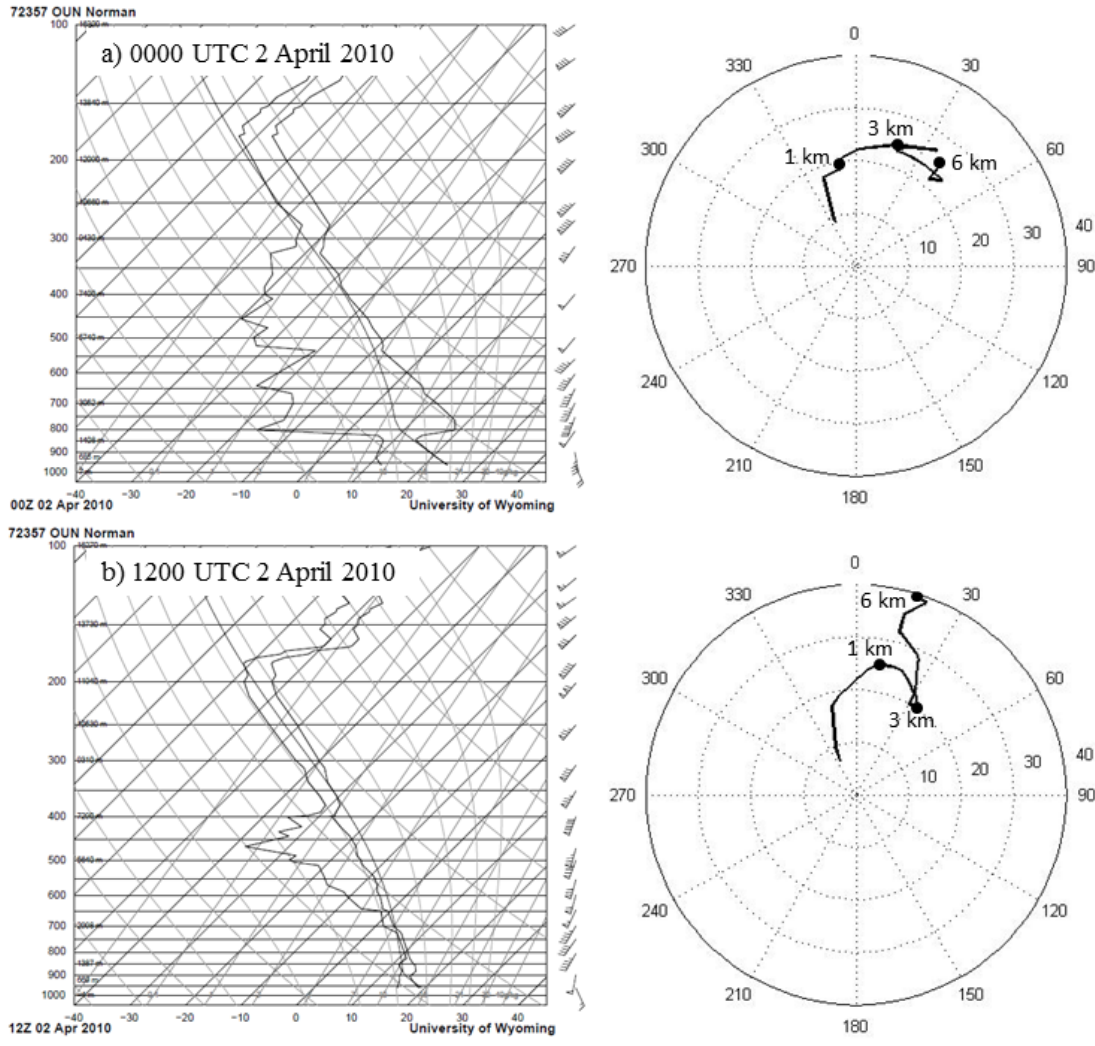


FIG. 3. Soundings from a) 0000 UTC and b) 1200 UTC on 2 April 2010 from Norman, OK. Pressure is plotted in hPa and temperature is plotted in °C. Wind barbs are shown in units of  $\text{m s}^{-1}$ , with one whole barb equal to  $5 \text{ m s}^{-1}$  and one pennant equal to  $25 \text{ m s}^{-1}$ . Hodographs for wind observations in the lowest six kilometers of soundings are shown to the right, with wind speeds shown in  $\text{m s}^{-1}$  and small numbers indicating height above ground level.

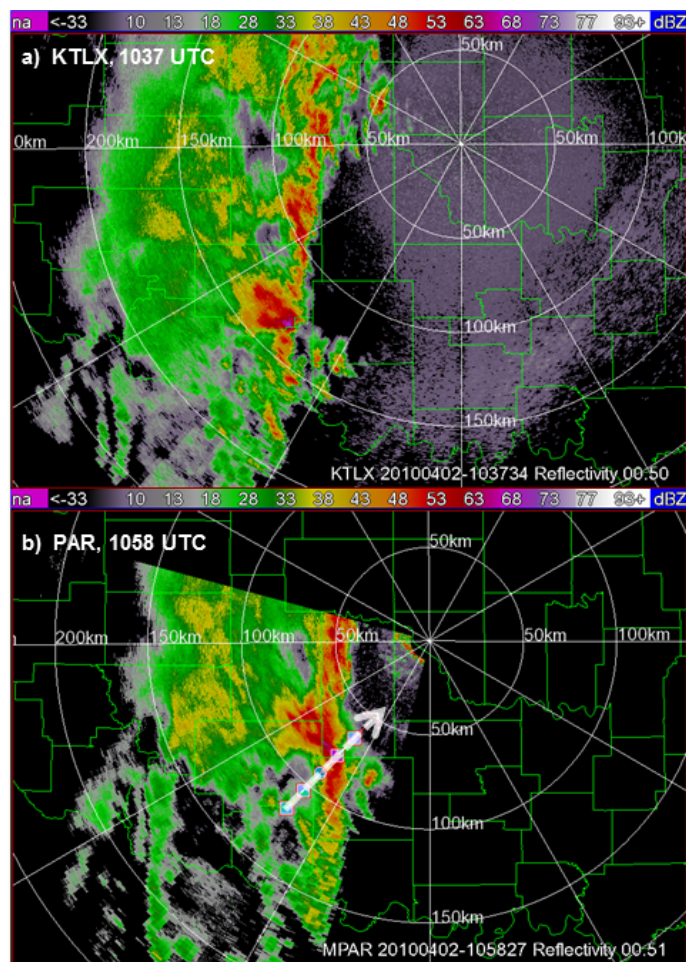


FIG. 4. a) KTLX  $0.5^\circ$  reflectivity at 1037 UTC 2 April 2010. b) PAR  $0.5^\circ$  reflectivity at 1058 UTC 2 April 2010. In b), dashed line shows cross section location discussed in PAR analysis section. In both images, Oklahoma counties are outlined in green, and range rings for each radar are shown in increments of 50 km.

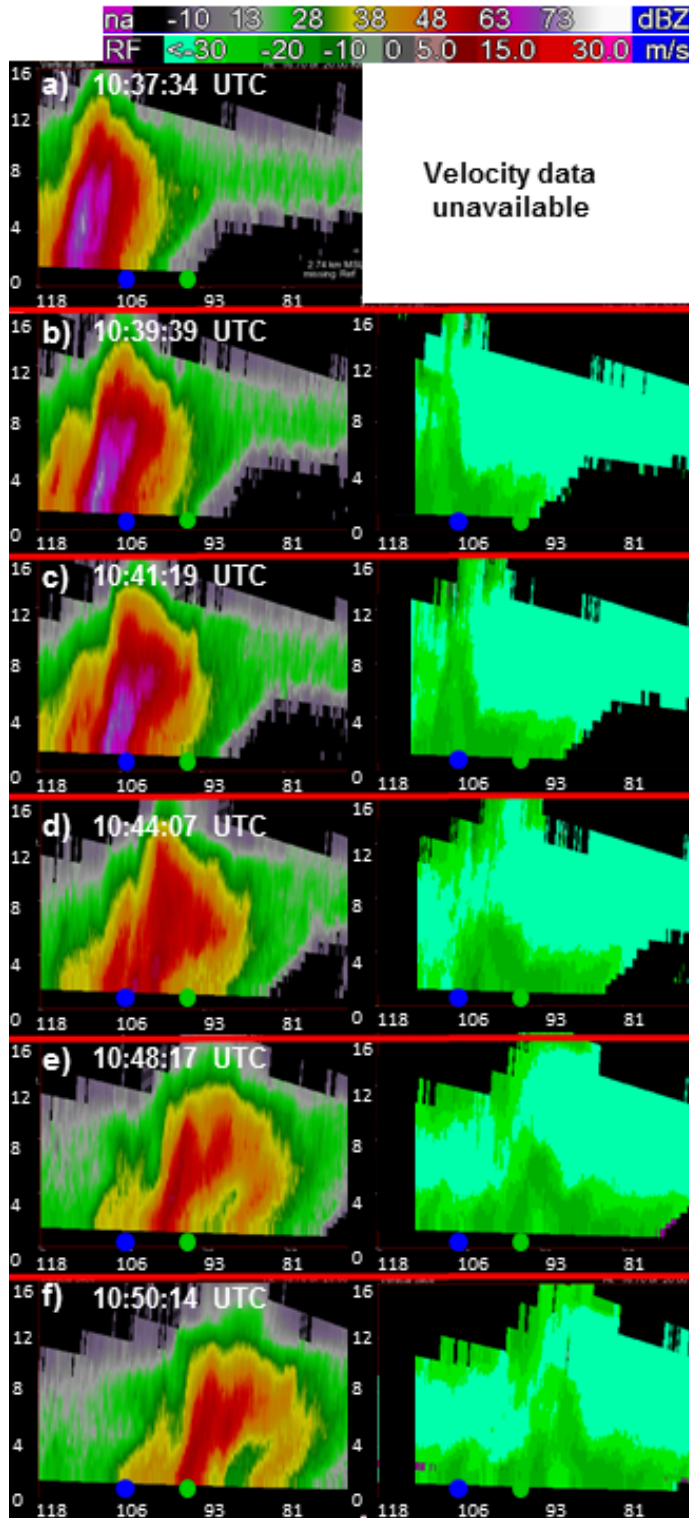


FIG. 5. PAR northeast-southwest reflectivity (left) and velocity (right) vertical cross sections. Location of cross section shown in Fig. 4. Decreasing numbers on the x-axis indicate distance from the PAR in km. Blue and green circles denote approximate locations of wind and hail reports, respectively, as discussed in the text. a) 10:37:34 UTC b) 10:39:39 UTC c) 10:41:19 UTC d) 10:44:07 UTC e) 10:48:17 UTC f) 10:50:14 UTC on 2 April 2010.

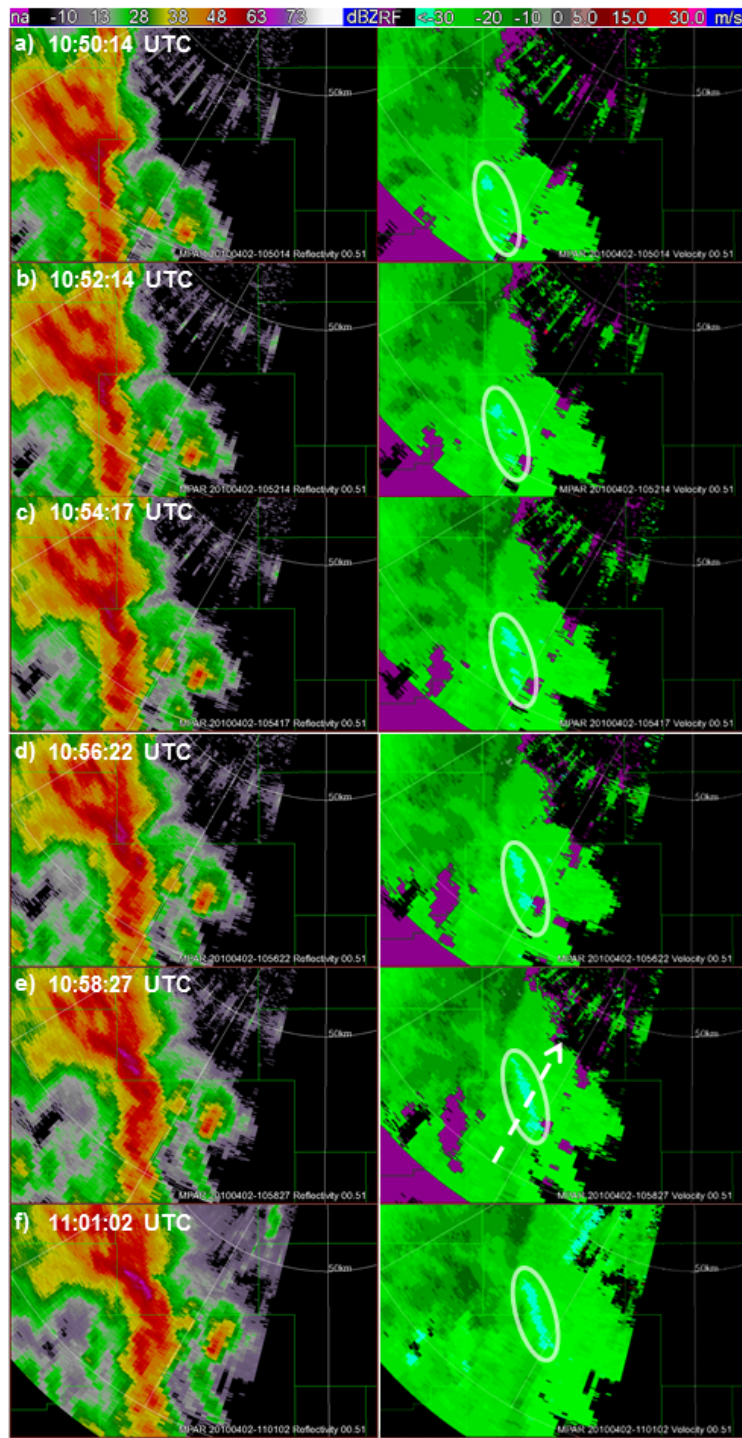


FIG. 6. PAR  $0.5^\circ$  reflectivity (left) and velocity (right) PPI scans. Oklahoma counties are outlined in green and range rings for the PAR are shown in increments of 50 km, with the first range ring corresponding to a range of 50 km. In velocity images, white circles indicate intensifying outflow. Radial spikes seen in images are the result of sidelobe echoes. White arrow in e) denotes location of cross section in Fig. 7. a) 10:50:14 UTC b) 10:52:14 UTC c) 10:54:17 UTC d) 10:56:22 UTC e) 10:58:27 UTC f) 11:01:02 UTC.

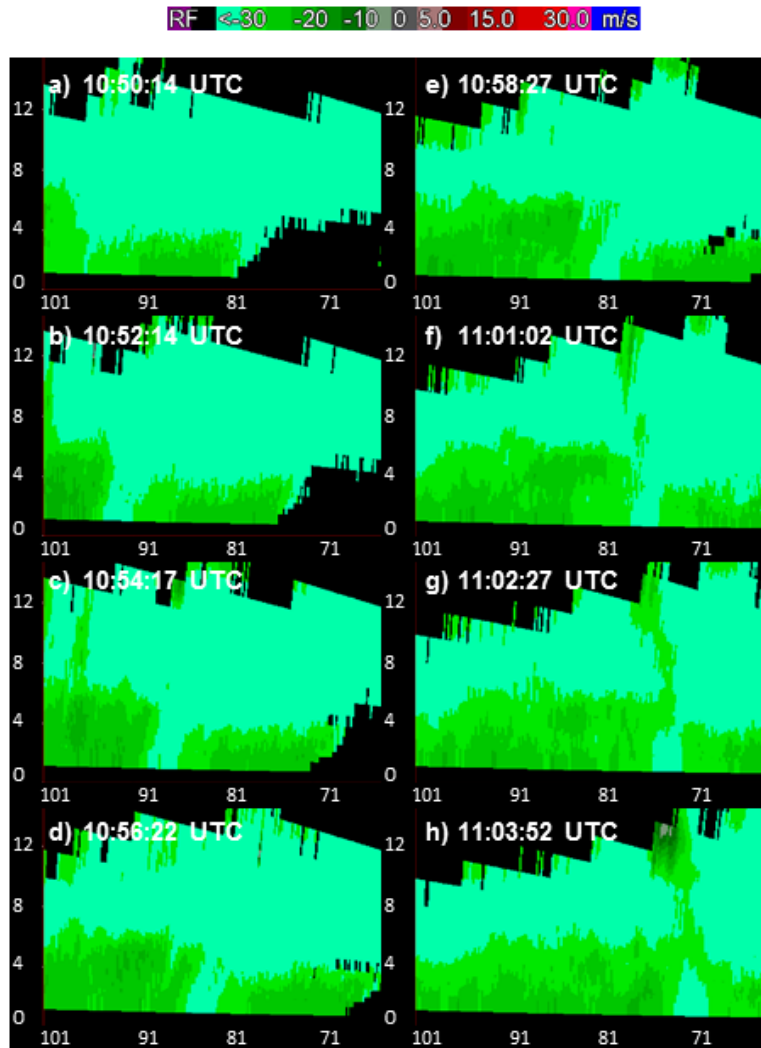


FIG. 7. PAR northeast-southwest velocity vertical cross sections. Decreasing numbers on the x-axis indicate distance from the PAR in km. Location of cross section is shown in Fig. 6e.

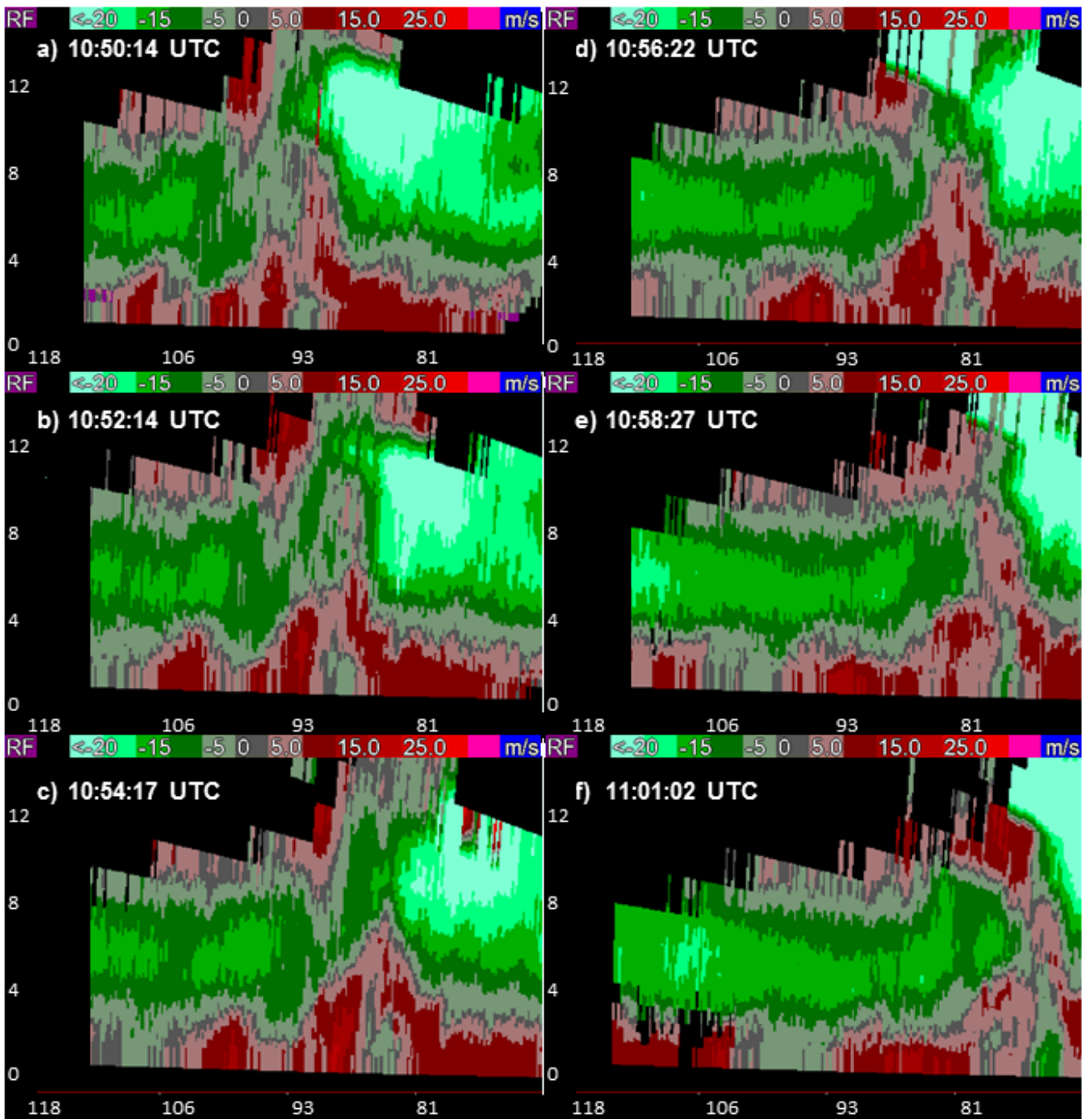


FIG. 8. PAR northeast-southwest storm-relative motion vertical cross section. Location of cross section shown in Fig. 4. Decreasing numbers on the x-axis indicate distance from the PAR in km. a) 10:50:14 UTC b) 10:52:14 UTC c) 10:54:17 UTC d) 10:56:22 UTC e) 10:58:27 UTC f) 11:01:02 UTC.

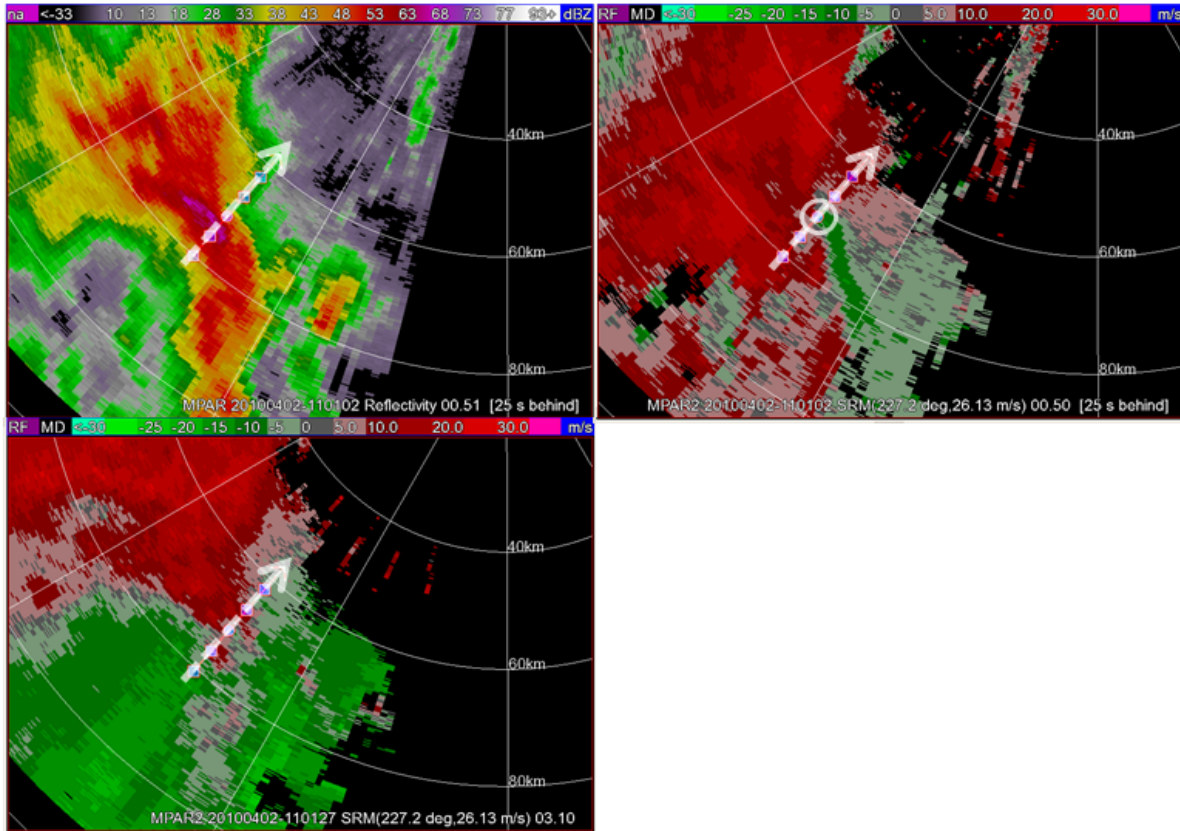


FIG. 9. PAR 0.5° reflectivity (top left), 0.5° storm-relative motion (top right), and 3.07° storm-relative motion (bottom left) PPI scans at 11:01:02 UTC. Dashed line shows location of cross sections in Figs. 10 and 11 at 11:01:02 UTC. Range rings for the PAR are shown in white and Rush Springs circulation is indicated by white circle in 0.5° storm-relative motion image. At this time, the 3.07° elevation angle was sampling the QLCS at  $\sim 4.2$  km ARL.

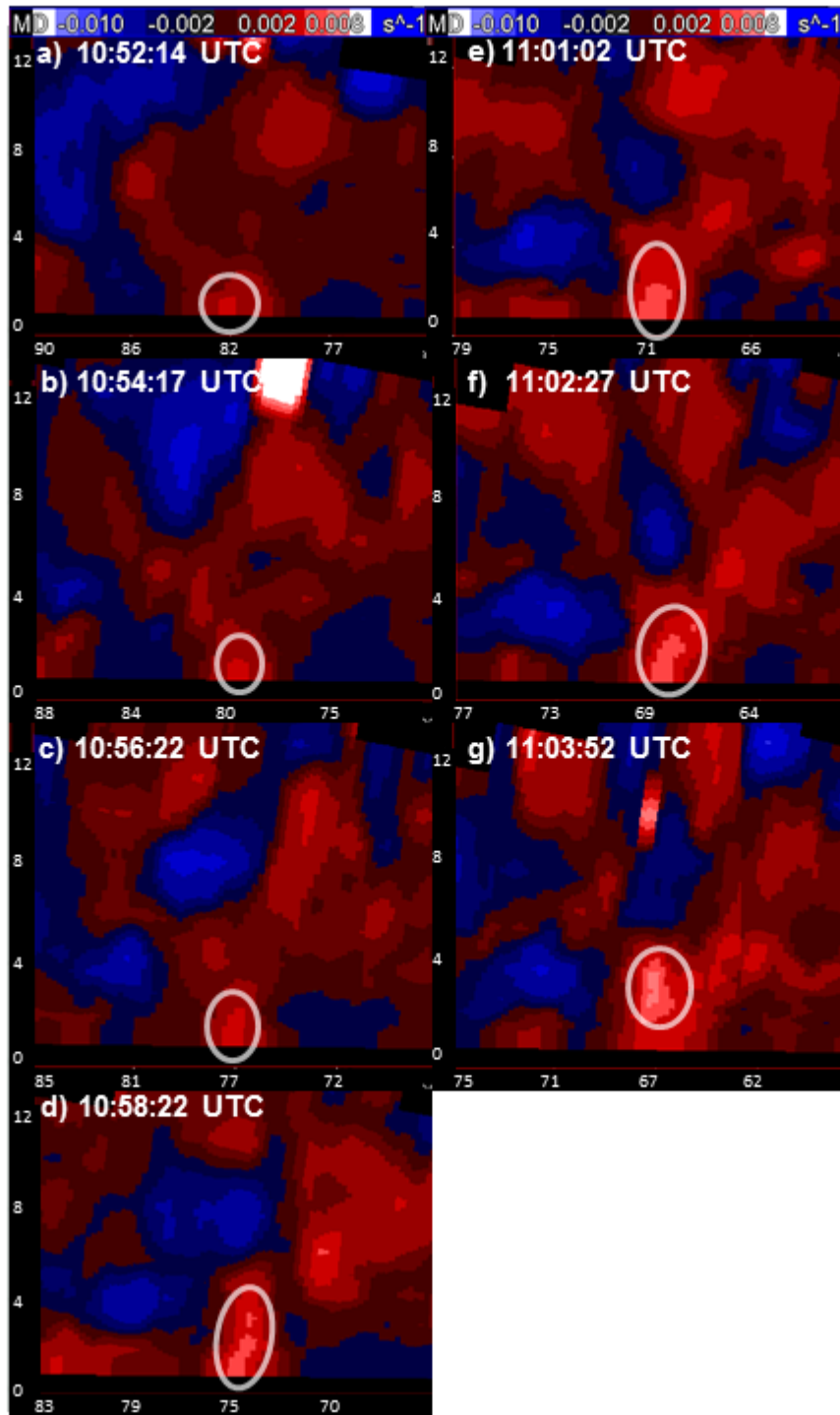


FIG. 10. PAR northeast-southwest oriented azimuthal shear vertical cross section. Shear was calculated using the local, linear least squares derivatives (LLSD) method (Smith and Elmore 2004). Location of cross section at 1101 UTC shown in Fig. 9. Cross section was centered on azimuthal shear maximum and taken along the radar beam axis. Decreasing numbers on the x-axis indicate distance from the PAR in km. White oval indicates approximate region where azimuthal shear exceeds  $0.002 \text{ s}^{-1}$ . a) 10:52:14 UTC b) 10:54:17 UTC c) 10:56:22 UTC d) 10:58:27 UTC e) 11:01:02 UTC f) 11:02:27 UTC g) 11:03:52 UTC.

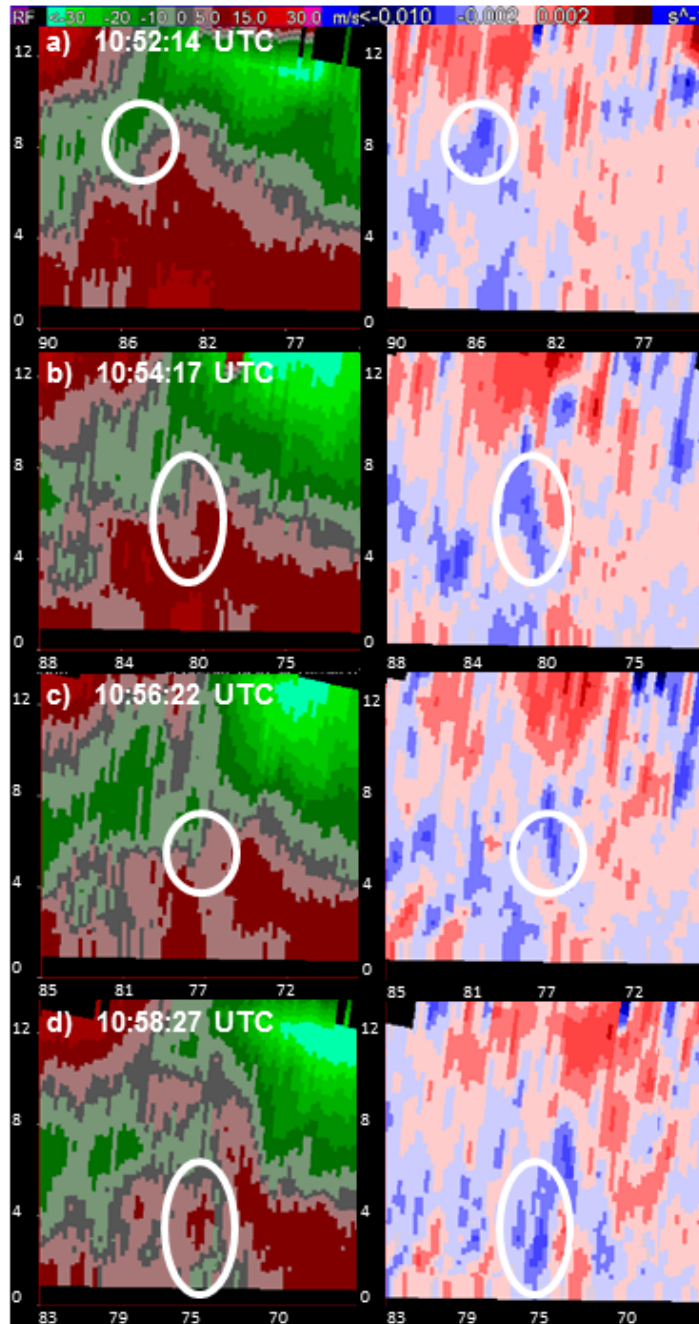


FIG. 11. PAR northeast-southwest oriented storm-relative motion (left) and divergence (right) vertical cross sections. Location of cross section at 1101 UTC shown in Fig. 9. Cross section was centered on azimuthal shear maximum and taken along the radar beam axis. Decreasing numbers on the x-axis indicate distance from the PAR in km. Divergence was calculated using the LLSD method (Smith and Elmore 2004). White oval indicates approximate region where divergence is less than  $-0.001 \text{ s}^{-1}$ . a) 10:52:14 UTC b) 10:54:17 UTC c) 10:56:22 UTC d) 10:58:27 UTC e) 11:01:02 UTC f) 11:02:27 UTC g) 11:03:52 UTC.

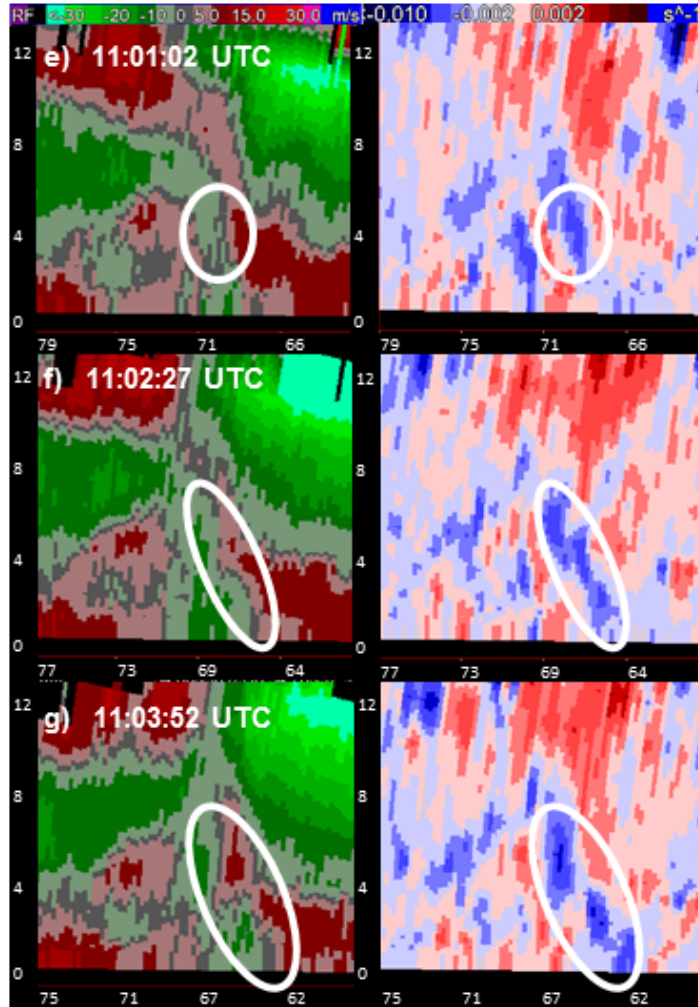


FIG. 11. (continued)

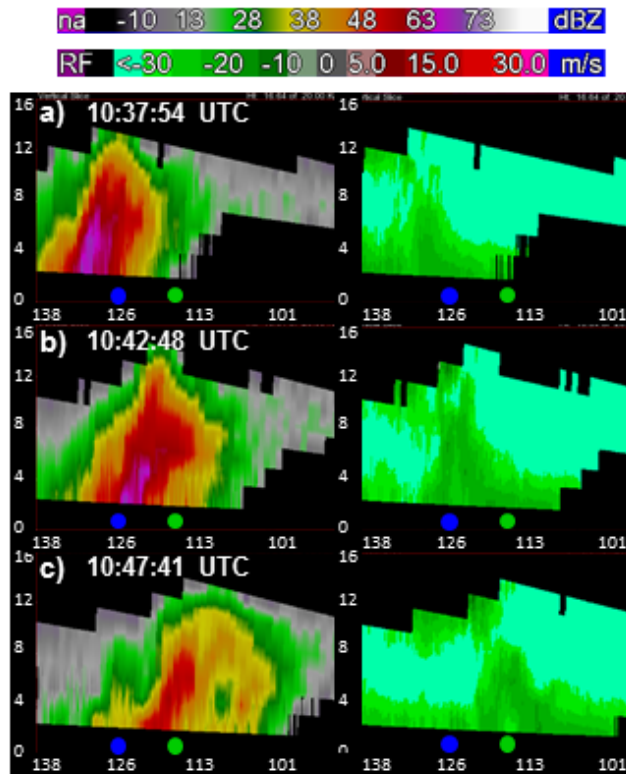


FIG. 12. As in Fig. 5, but for KTLX radar. Decreasing numbers on the x-axis indicate distance from KTLX in km. a) 10:37:54 UTC b) 10:42:48 UTC c) 10:47:41 UTC.

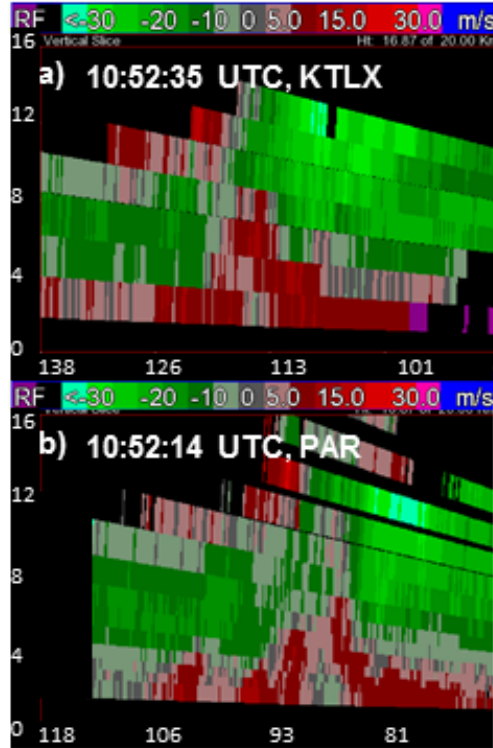


FIG. 13. KTLX and PAR northeast-southwest storm-relative motion vertical cross sections. Location of cross section shown in Fig. 4. Decreasing numbers on the x-axis indicate decreasing distance from the radars in km. Times refer to time of  $0.5^\circ$  elevation scan. a) KTLX, 10:52:35 UTC b) PAR, 10:52:14 UTC.

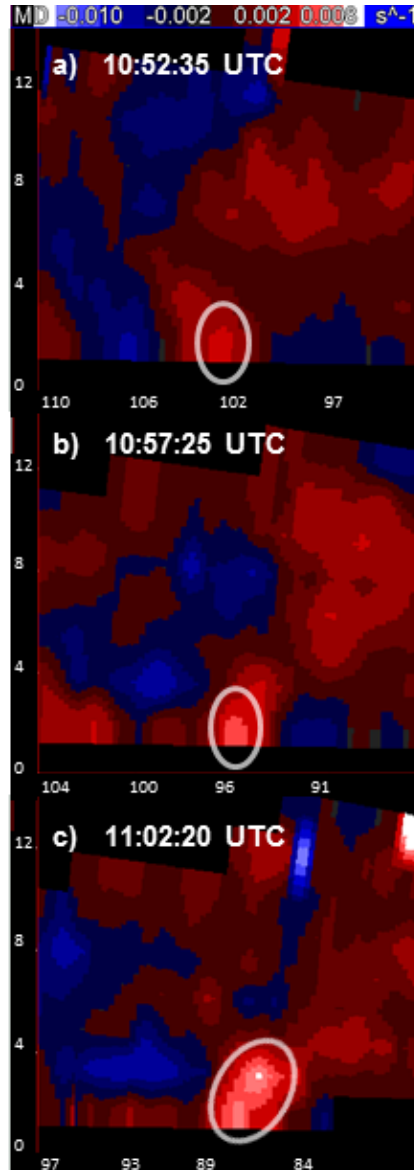


FIG. 14. As in Fig. 10, but for KTLX azimuthal shear. Decreasing numbers on the x-axis indicate distance from KTLX in km. a) 10:52:35 UTC b) 10:57:25 UTC c) 11:02:20 UTC.

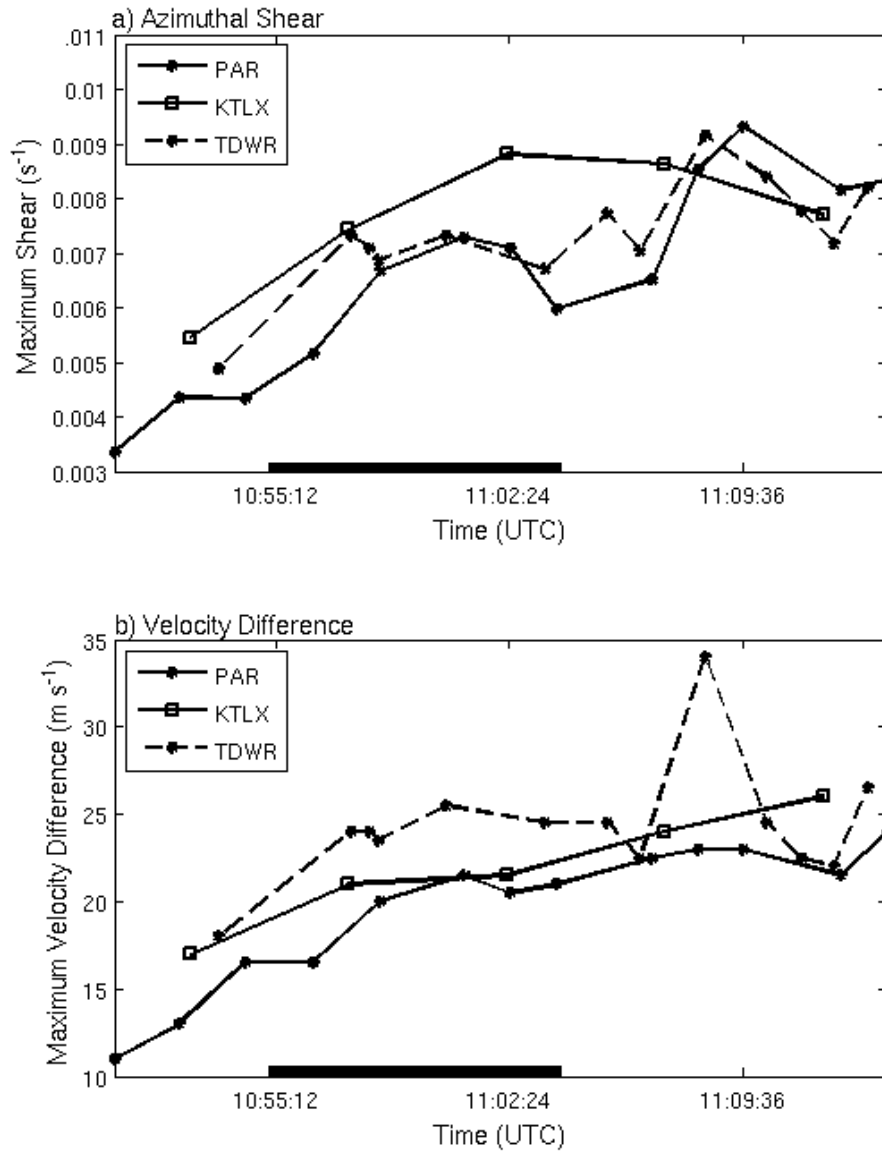


FIG. 15. Time series of maximum  $0.5^\circ$  a) azimuthal shear and b) velocity difference values along circulation path from PAR, KTLX and TDWR data. Maximum velocity difference was found by calculating the difference between the maximum and minimum velocity values at constant range within a 3-km search radius of each point. Black line indicates approximate circulation damage period. At 1102 UTC, the  $0.5^\circ$  elevation angles of PAR, KTLX, and TDWR were sampling the circulation at 0.9 km, 1.2 km, and 0.9 km ARL, respectively.

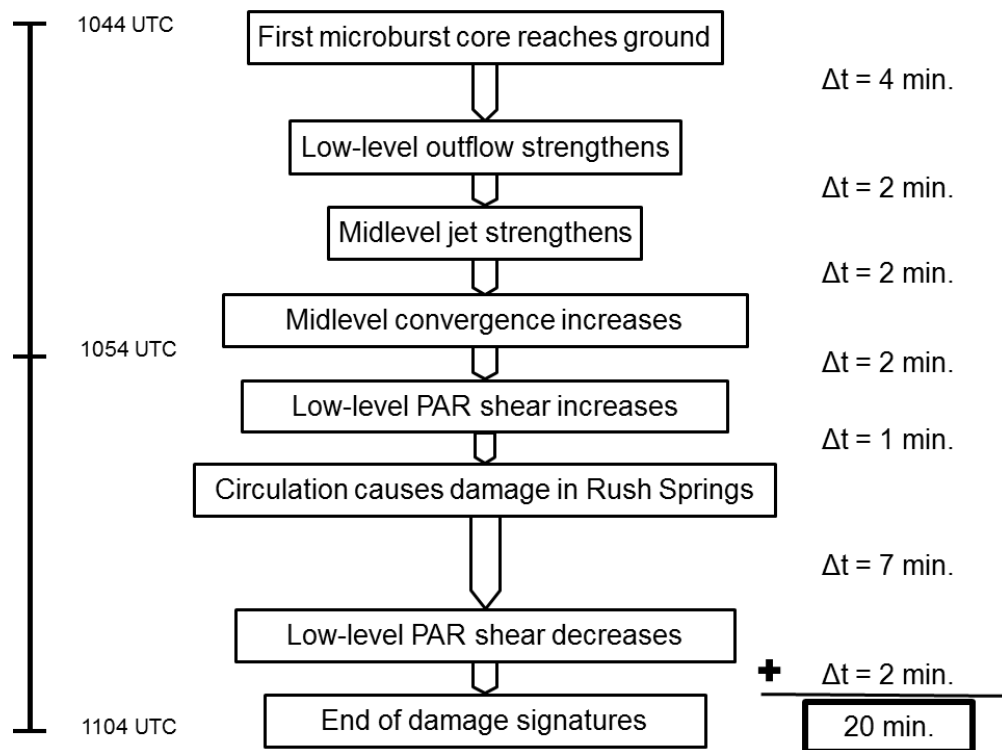


FIG. 16. Diagram depicting evolution of Rush Springs circulation as observed in PAR data. Time increases toward the bottom of the diagram.  $\Delta t$  is the time elapsed between the start times of subsequent radar-indicated signatures.